

# Analyzing and Guiding Zero-Shot Posterior Sampling in Diffusion Models

Roi Benita<sup>1</sup> Michael Elad<sup>2</sup> Joseph Keshet<sup>1</sup>

## Abstract

Recovering a signal from its degraded measurements is a long standing challenge in science and engineering. Recently, zero-shot diffusion based methods have been proposed for such inverse problems, offering a posterior sampling based solution that leverages prior knowledge. Such algorithms incorporate the observations through inference, often leaning on manual tuning and heuristics.

In this work we propose a rigorous analysis of such approximate posterior-samplers, relying on a Gaussianity assumption of the prior. Under this regime, we show that both the ideal posterior sampler and diffusion-based reconstruction algorithms can be expressed in closed-form, enabling their thorough analysis and comparisons in the spectral domain. Building on these representations, we also introduce a principled framework for parameter design, replacing heuristic selection strategies used to date. The proposed approach is method-agnostic and yields tailored parameter choices for each algorithm, jointly accounting for the characteristics of the prior, the degraded signal, and the diffusion dynamics. We show that our spectral recommendations differ structurally from standard heuristics and vary with the diffusion step size, resulting in a consistent balance between perceptual quality and signal fidelity.

## 1. Introduction

Linear inverse problems, a common task across many scientific fields, refer to the recovery of an unknown signal from its noisy, degraded measurements. Traditionally, supervised methods address this problem by learning direct mappings from observations to clean signals for a specific degradation model, using large paired datasets (Dong et al., 2015; Zhang

<sup>1</sup>Department of Electrical and Computer Engineering, Technion, Haifa, Israel <sup>2</sup>Department of Computer Science, Technion, Haifa, Israel . Correspondence to: Roi Benita <roibenita@campus.technion.ac.il>.

et al., 2016; Saharia et al., 2022). However, real-world applications often involve more varied scenarios, requiring general frameworks beyond task-specific training. Building on this need, recent advances in diffusion models have proposed zero-shot posterior sampling methods applicable across different degradation settings without retraining.

In this unsupervised setting, sampling is guided by a pre-trained diffusion model learned on the clean signal manifold, with methods differing in how observations are incorporated during inference. One perspective steers the synthesis process by explicitly projecting intermediate samples onto geometric constraints induced by the measurements (Choi et al., 2021; Wang et al., 2022; Kawar et al., 2022; Zhu et al., 2023). Another common approach adopts a Bayesian formulation, where posterior estimation includes a likelihood term (Bansal et al., 2023; Xu & Chi, 2024; Chung et al., 2022a; Song et al., 2023). The likelihood is method dependent, reflects the degradation model, and guides the denoising process toward consistency with the measurements. Throughout this work, we adopt a unified prior-likelihood terminology (Daras et al., 2024).

Despite the remarkable success of this methods, A fundamental question is how to determine the relative weight between both forces, the likelihood and the prior information. One possible option is using small guidance step sizes, allowing sampling to be gradually influenced by the observations (Chung et al., 2022a; Yu et al., 2023; Bansal et al., 2023). However, this typically requires many diffusion steps and slows inference (Yang et al., 2024; Zhang et al., 2025). Alternatively, using large guidance weights can lead to unstable or unpredictable behavior (He et al., 2023).

In the absence of a principled solution, existing methods often choose these weighting parameters manually or heuristically (Daras et al., 2024). One approach relies on empirically chosen, dataset-dependent scaling factors adjusted based on the discrepancy with the observations (Chung et al., 2022a). Another approach instead uses globally defined parameters determined by the diffusion noise levels (Song et al., 2023; Bansal et al., 2023). Notably, current design choices often do not jointly account for the interaction between prior characteristics, sampling dynamics, and the observed information. This can affect method performance, reflected in the balance between sample naturalness and

measurement fidelity (Blau & Michaeli, 2018), and may lead to longer sampling trajectories.

In this work, we propose a structured analysis of zero-shot posterior samplers, inspired by the spectral perspective of (Benita et al., 2025). Under a Gaussian prior assumption, we derive a closed-form expressions for the ideal posterior sampler and diffusion-based training-free reconstruction methods. The resulting analytical representations provides a sound basis for posterior-level comparison across existing samplers. In addition, we introduce a principled way of designing the guidance weighting parameters while jointly accounts for the prior characteristics, the degraded observations, and the diffusion dynamics. Finally, we validate our framework on real-world datasets, including FFHQ (Karras et al., 2019) and ImageNet (Deng et al., 2009), comparing our spectral recommendations with existing heuristics and evaluating image naturalness and measurement fidelity across varied diffusion step sizes.

In summary, our contributions are the following: (i) We introduce a structured spectral analysis of zero-shot posterior sampling methods, providing a unified view under a common analytical framework. (ii) Under a Gaussian prior assumption, we derive closed-form expressions for the output distributions of the ideal posterior sampler and diffusion-based training-free reconstruction methods, enabling their direct posterior-level comparison and analysis. (iii) We formulate a principled, method-agnostic optimization problem for selecting guidance weighting parameters which jointly accounts for the prior characteristics, the degraded observations, and the diffusion dynamics. We demonstrate how it can be instantiated across different posterior sampling algorithms and solved either for individual realizations or efficiently for a general degradation system. (iv) We evaluate our proposed spectral recommendations relative to existing heuristics for posterior sampling, considering both averaged and fixed-observation settings, and assessing sample naturalness, measurement fidelity, and dependence on the number of diffusion steps.

## 2. Background

### 2.1. Linear Inverse Problems

A general linear inverse problem is defined as:

$$\mathbf{y} = \mathbf{H}\mathbf{x} + \mathbf{n}, \quad (1)$$

Where the goal is to recover an unknown signal  $\mathbf{x} \in \mathbb{R}^d$  from a degraded observation  $\mathbf{y} \in \mathbb{R}^m$ , Wherein  $\mathbf{H} \in \mathbb{R}^{m \times d}$  is a known linear degradation matrix, and  $\mathbf{n} \sim \mathcal{N}(\mathbf{0}, \sigma_y^2 \mathbf{I})$  denotes i.i.d. additive Gaussian noise. A common property of these problems is the loss of information induced by the degradation operator  $\mathbf{H}$ , making perfect recovery of  $\mathbf{x}$  from  $\mathbf{y}$  generally impossible and rendering the problem ill-posed.

### 2.2. Diffusion Models

Diffusion models form a generative framework that transforms a simple normal distribution into a target data distribution  $p(\mathbf{x}_0)$ , enabling the synthesis of samples  $\mathbf{x}_0 \in \mathbb{R}^d$ . The diffusion process consists of two Markovian paths, the *forward* and *reverse* processes, each comprising a sequence of  $T$  latent variables. The *forward* process, introduced in DDPM (Ho et al., 2020), gradually corrupts a clean signal  $\mathbf{x}_0$  by additive Gaussian noise:

$$\mathbf{x}_t = \sqrt{\alpha_t} \mathbf{x}_{t-1} + \sqrt{1 - \alpha_t} \epsilon_t, \quad (2)$$

where  $\{\alpha_t\}_{t=1}^T$  defines a monotonically decreasing noise schedule and  $\epsilon_t \sim \mathcal{N}(\mathbf{0}, \mathbf{I})$ . A key property of the forward process is its marginal distribution at time step  $t$ :

$$\mathbf{x}_t = \sqrt{\bar{\alpha}_t} \mathbf{x}_0 + \sqrt{1 - \bar{\alpha}_t} \epsilon \quad \epsilon \sim \mathcal{N}(\mathbf{0}, \mathbf{I}), \quad (3)$$

with  $\bar{\alpha}_t = \prod_{i=1}^t \alpha_i$ , while for sufficiently large  $T$ ,  $\mathbf{x}_T \sim \mathcal{N}(\mathbf{0}, \mathbf{I})$ .

The *reverse* process aims to reconstruct  $\mathbf{x}_0$  from  $\mathbf{x}_T$  by iteratively denoising it. Extending the stochastic DDPM formulation (Ho et al., 2020), the authors of (Song et al., 2021) introduced DDIM, a deterministic inference framework that enables accelerated sampling. As a result, the inference trajectory is defined by:

$$\begin{aligned} \mathbf{x}_{s-1} = \sqrt{\bar{\alpha}_{s-1}} & \left( \frac{\mathbf{x}_s - \sqrt{1 - \bar{\alpha}_s} \cdot \epsilon_\theta(\mathbf{x}_s, s)}{\sqrt{\bar{\alpha}_s}} \right) \\ & + \sqrt{1 - \bar{\alpha}_{s-1} - \sigma_s^2} \cdot \epsilon_\theta(\mathbf{x}_s, s) + \sigma_s \epsilon_s, \end{aligned} \quad (4)$$

where  $s \in \{0, 1, \dots, S\}$  indexes a subsequence of diffusion steps,  $\sigma_s = \eta \sqrt{(1 - \alpha_{s-1})/(1 - \alpha_s)} \sqrt{1 - \alpha_s/\alpha_{s-1}}$ , and  $\epsilon_\theta(\mathbf{x}_s, s)$  denotes a neural network parameterized by  $\theta$  that estimates  $\epsilon$  from a given  $\mathbf{x}_s$  at time  $s$ . When  $\eta = 1$ , the generative process reduces to DDPM, whereas  $\eta = 0$  yields the deterministic DDIM sampler. In this work, we denote the set of noise schedule parameters by  $\bar{\alpha} = \{\bar{\alpha}_t\}_{t=1}^T$  for DDPM and  $\bar{\alpha} = \{\bar{\alpha}_s\}_{s=1}^S$  for DDIM.

### 2.3. training-free Diffusion-based methods for inverse problems

Training-free diffusion-based methods address inverse problems by adapting a pretrained diffusion prior at inference time, thereby avoiding task-specific retraining (Daras et al., 2024). A first class of methods relies on projection-based updates, in which the standard sampling process is modified to enforce data consistency at each time step (Wang et al., 2022; Kawar et al., 2022; Choi et al., 2021). In contrast, Bayesian methods (Bansal et al., 2023; Xu & Chi, 2024; Chung et al., 2022a; Song et al., 2023) formulate inverse problems as posterior inference tasks by explicitly combining a pretrained diffusion prior with a measurement

likelihood, leading to the following score decomposition:

$$\nabla_{\mathbf{x}_t} \log p_t(\mathbf{x}_t | \mathbf{y}) = \nabla_{\mathbf{x}_t} \log p_t(\mathbf{x}_t) + \nabla_{\mathbf{x}_t} \log p_t(\mathbf{y} | \mathbf{x}_t) \quad (5)$$

Based on the Tweedie's formula (Efron, 2011), the prior score is obtained from the learned estimator as:

$$\nabla_{\mathbf{x}_t} \log p_t(\mathbf{x}_t) \approx -\frac{1}{\sqrt{1 - \bar{\alpha}_t}} \boldsymbol{\epsilon}_\theta(\mathbf{x}_t, t) \quad (6)$$

The likelihood term is approximated in a method-dependent manner to guide sampling toward consistency with the measurements. A common approach is DPS (Chung et al., 2022a), which adopts a deterministic approximation by marginalizing over the clean signal using the denoiser output  $p(\mathbf{y} | \mathbf{x}_t) \simeq p(\mathbf{y} | \hat{\mathbf{x}}_0)$  where  $\hat{\mathbf{x}}_0 := \mathbb{E}[\mathbf{x}_0 | \mathbf{x}_t]$ . Using this likelihood within the deterministic DDIM (Song et al., 2021) formulation, leads to the following update rule:

$$\begin{aligned} \mathbf{x}_{s-1} = & \sqrt{\bar{\alpha}_{s-1}} \hat{\mathbf{x}}_0 + \sqrt{1 - \bar{\alpha}_{s-1}} \boldsymbol{\epsilon}_\theta(\mathbf{x}_s, s) \\ & - \zeta_s \nabla_{\mathbf{x}_s} \|\mathbf{y} - \mathbf{H}\hat{\mathbf{x}}_0\|_2^2 \end{aligned} \quad (7)$$

where  $\zeta_s = \zeta' / |\mathbf{y} - \mathbf{H}\hat{\mathbf{x}}_0(\mathbf{x}_s)|$  is a heuristic reweighting term which scales the guidance step size inversely with the measurement error norm, and  $\zeta'$  is a user-defined constant. Alternatively, IIGDM (Song et al., 2023) models  $p(\mathbf{x}_0 | \mathbf{x}_t)$  as a Gaussian distribution with mean  $\hat{\mathbf{x}}_0$  and variance  $r_t^2$ , which controls the uncertainty at diffusion step  $t$ . This yields the likelihood approximation  $p_t(\mathbf{y} | \mathbf{x}_t) \approx \mathcal{N}(\mathbf{H}\hat{\mathbf{x}}_0, r_t^2 \mathbf{H}\mathbf{H}^T + \sigma_y^2 \mathbf{I})$  where the variance parameter  $r_t$  is also incorporated as a weighting term in the deterministic DDIM update:

$$\begin{aligned} \mathbf{x}_{s-1} = & \sqrt{\bar{\alpha}_{s-1}} \hat{\mathbf{x}}_0 + \sqrt{1 - \bar{\alpha}_{s-1}} \boldsymbol{\epsilon}_\theta(\mathbf{x}_s, s) \\ & + r_s^2 \nabla_{\mathbf{x}_s} (\hat{\mathbf{x}}_0)^T \mathbf{H}^T ((r_s^2 \mathbf{H}\mathbf{H}^T + \sigma_y^2 \mathbf{I})^{-1})^T (\mathbf{y} - \mathbf{H}\hat{\mathbf{x}}_0) \end{aligned} \quad (8)$$

Specifically,  $r_s$  is defined heuristically according to the diffusion noise schedule  $r_s = \sqrt{1 - \bar{\alpha}_s}$ . Throughout the rest of the paper, we denote by  $\zeta$  and  $r$  the sets of heuristic hyperparameters  $\{\zeta_s\}_{s=1}^S$  and  $\{r_s\}_{s=1}^S$ , respectively.

### 3. Guided zero-shot posterior samplers

In this section, we bring diffusion-based zero-shot posterior sampling methods together under a unified spectral perspective. Our framework is method-agnostic and builds upon principles from (Benita et al., 2025) to enable simplified analysis and principled design of the underlying heuristics. We use DPS (Chung et al., 2022a) as a representative instance and further demonstrate our framework with IIGDM (Song et al., 2023) in Appendix G. Notably, the proposed approach naturally extends to other samplers within this class (Wang et al., 2022; Zhu et al., 2023).

### 3.1. The Optimal Denoiser for a Gaussian Prior

As reviewed in Section 2.3, training-free posterior samplers leverage a pretrained denoiser to incorporate prior information during the inference phase. Following (Benita et al., 2025), we assume a Gaussian prior on the clean signal,  $\mathbf{x}_0 \sim \mathcal{N}(\boldsymbol{\mu}_0, \boldsymbol{\Sigma}_0)$ , where  $\boldsymbol{\mu}_0 \in \mathbb{R}^d$  and  $\boldsymbol{\Sigma}_0 \in \mathbb{R}^{d \times d}$ . Under this modeling choice, for a noisy signal  $\mathbf{x}_t$  at diffusion step  $t$  and noise schedule  $\bar{\alpha}$ , the optimal denoiser admits the following closed-form expression:

$$\begin{aligned} \mathbf{x}_0^* = & (\bar{\alpha}_t \boldsymbol{\Sigma}_0 + (1 - \bar{\alpha}_t) \mathbf{I})^{-1} \\ & (\sqrt{\bar{\alpha}_t} \boldsymbol{\Sigma}_0 \mathbf{x}_t + (1 - \bar{\alpha}_t) \boldsymbol{\mu}_0) \end{aligned} \quad (9)$$

### 3.2. Reverse Process Formulation

We next describe the DPS (Chung et al., 2022a) sampling procedure under the Gaussian setting. For brevity, we highlight the key steps using the DDIM (Song et al., 2021) formulation, which facilitates an accelerated sampling framework, while the full derivation is provided in Appendix F. Based on the marginal relation in (3), the deterministic update from (7) can be expressed in terms of the optimal denoiser as follows:

$$\mathbf{x}_{s-1} = a_s \mathbf{x}_s + b_s \mathbf{x}_0^* - \zeta_s \nabla_{\mathbf{x}_s} \|\mathbf{y} - \mathbf{H}\mathbf{x}_0^*\|_2^2 \quad (10)$$

where  $\mathbf{y} = \mathbf{H}\mathbf{x}_0 + \mathbf{n}$  denotes the linear degradation model,  $a_s$  and  $b_s$  are determined by the noise schedule  $\bar{\alpha}$ , and  $\zeta_s$  is the corresponding likelihood weight.

### 3.3. Migrating to spectral domain

Inspired by (Benita et al., 2025), we adopt a spectral perspective, which allows a simplified analysis of the diffusion dynamics. In particular, we consider the case where the covariance matrix  $\boldsymbol{\Sigma}_0$  is shift-invariant, a reasonable assumption for natural images (Unser, 1984; Freirich et al., 2021), and the degradation operator  $\mathbf{H}$  shares this property. This structure induces diagonalization in the Fourier basis and makes the analysis relevant for common linear inverse problems such as deblurring and denoising.

Under this setting, the prior distribution in the spectral domain remains Gaussian,  $\mathbf{x}_0^{\mathcal{F}} \sim \mathcal{N}(\boldsymbol{\mu}_0^{\mathcal{F}}, \boldsymbol{\Lambda}_0)$ , where  $\boldsymbol{\mu}_0^{\mathcal{F}}$  is the transformed mean vector, and  $\boldsymbol{\Lambda}_0 \in \mathbb{R}^{d \times d}$  is a positive semidefinite diagonal matrix containing the eigenvalues of  $\boldsymbol{\Sigma}_0$ , denoted by  $\{\lambda_i\}_{i=1}^d$ . Furthermore,  $\mathbf{H} \in \mathbb{R}^{d \times d}$  admits a diagonal spectral representation  $\boldsymbol{\Lambda}_h$ , whose diagonal entries are the eigenvalues of  $\mathbf{H}$ , with  $\boldsymbol{\Lambda}_h^*$  denoting its complex conjugate. Accordingly, the posterior  $p(\mathbf{x}_0^{\mathcal{F}} | \mathbf{y}^{\mathcal{F}})$  remains Gaussian and admits a closed-form expression in the spectral domain, with  $\mathbf{y}^{\mathcal{F}}$  denotes the spectral domain measurements. A detailed derivation is provided in Appendix D.

By projecting Equation (10) onto the unitary Fourier basis  $\mathbf{F} \in \mathbb{C}^{d \times d}$ , we obtain the following relation between con-

secutive diffusion steps in the spectral domain, where the superscript  $\mathcal{F}$  denotes the Fourier-domain representation.

$$\begin{aligned} \mathbf{x}_{s-1}^{\mathcal{F}} = & [a_s + b_s c_s - 2\zeta_s c_s \mathbf{\Lambda}_{h^*} \mathbf{\Lambda}_h c_s] \mathbf{x}_s^{\mathcal{F}} \\ & + [2\zeta_s c_s \mathbf{\Lambda}_{h^*}] \mathbf{y}^{\mathcal{F}} + [b_s d_s - 2\zeta_s c_s \mathbf{\Lambda}_{h^*} \mathbf{\Lambda}_h d_s] \boldsymbol{\mu}_0^{\mathcal{F}} \end{aligned} \quad (11)$$

Here,  $a_s$  and  $b_s$  are diagonal matrices determined by the noise schedule  $\bar{\alpha}$ , and  $c_s$ ,  $d_s$  further reflect the spectral properties encoded in  $\mathbf{\Lambda}_0$ . Definitions are provided in Appendix F.2.

Using the diagonalization property of Equation (11), the update decouples into  $d$  independent scalar equations, which can be recursively substituted. This yields a closed-form expression for the estimated output signal over  $S$  diffusion steps.

$$\hat{\mathbf{x}}_{0,\text{DPS}}^{\mathcal{F}} = \mathbf{D}_1 \mathbf{x}_S^{\mathcal{F}} + \mathbf{D}_2 \mathbf{y}^{\mathcal{F}} + \mathbf{D}_3 \boldsymbol{\mu}_0^{\mathcal{F}} \quad (12)$$

Where  $\mathbf{D}_1$ ,  $\mathbf{D}_2$ , and  $\mathbf{D}_3$  are diagonal matrices whose entries are determined by the noise schedule  $\bar{\alpha}$ , the number of diffusion steps  $S$ , and the spectral characteristics of the prior  $\mathbf{\Lambda}_0$ . Interestingly, Equation (12) can be interpreted as a set of  $d$  scalar *transfer functions* mapping the Gaussian input noise  $\mathbf{x}_S \sim \mathcal{N}(\mathbf{0}, \mathbf{I})$  and the noisy, degraded measurement  $\mathbf{y}^{\mathcal{F}}$  to the clean output estimate.

Finally, from a probabilistic perspective, the resulting posterior distribution is

$$\hat{\mathbf{x}}_{0,\text{DPS}}^{\mathcal{F}} \mid \mathbf{y}^{\mathcal{F}} \sim \mathcal{N}(\mathbf{D}_2 \mathbf{y}^{\mathcal{F}} + \mathbf{D}_3 \boldsymbol{\mu}_0^{\mathcal{F}}, \mathbf{D}_1^2). \quad (13)$$

This reconstruction captures information from the prior structure, the diffusion dynamics and the measurement  $\mathbf{y}^{\mathcal{F}}$ , with the latter incorporated through DPS-based update, contributing to the posterior via its first-order statistics. Additional details and definitions are provided in Appendix F.2.

### 3.4. Optimal Posterior Sampling Weights

By leveraging the closed-form expressions for the reconstructed distributions such as (13), we further analyze the dynamics of diffusion-based posterior sampling methods from a spectral perspective. A key aspect relates to the design choices of the prior-likelihood weighting heuristics. We consider a setting with a prior covariance matrix  $\mathbf{\Sigma}_0$ , characterized by eigenvalues  $\{\lambda_i\}_{i=1}^d$ , a fixed linear degradation matrix  $\mathbf{H}$ , an observation  $\mathbf{y}$ , and a diffusion process with  $S$  diffusion steps and noise schedule  $\bar{\alpha}$ . Our objective is to bring the estimated probability density induced by such posterior sampling methods as close as possible to the true posterior distribution. Accordingly, we seek a set of weights  $\boldsymbol{\zeta}$  that minimizes a discrepancy measure  $\mathcal{D}$  between the estimated reconstructed distribution,  $p(\hat{\mathbf{x}}_{0,\text{DPS}}^{\mathcal{F}} \mid \mathbf{y}^{\mathcal{F}}; \boldsymbol{\zeta}, \bar{\alpha})$ , and the true posterior distribution  $p(\mathbf{x}_0^{\mathcal{F}} \mid \mathbf{y}^{\mathcal{F}})$ , leading to the

following optimization problem.<sup>1</sup>

$$\boldsymbol{\zeta}^* = \arg \min_{\boldsymbol{\zeta}} \mathcal{D}(p(\hat{\mathbf{x}}_{0,\text{DPS}}^{\mathcal{F}} \mid \mathbf{y}^{\mathcal{F}}; \boldsymbol{\zeta}, \bar{\alpha}), p(\mathbf{x}_0^{\mathcal{F}} \mid \mathbf{y}^{\mathcal{F}})) \quad (14)$$

Choosing the discrepancy measure  $\mathcal{D}$  is a key design choice, as it governs how measurement fidelity is balanced with prior information and ultimately shapes the trade-off between perceptual quality and distortion (Blau & Michaeli, 2018). In principle, for a given observation  $\mathbf{y}$ , one could define various discrepancy measures  $\mathcal{D}$  between the corresponding posterior distributions, such as the *Wasserstein-2* (Arjovsky et al., 2017) or *KL divergence* (Kullback & Leibler, 1951). However, we adopt a more general formulation based on the *Wasserstein-2* distance, referred to as the *averaged Wasserstein distance* and denoted by:

$$[\mathcal{D}_{W_2}^2]_{\text{Avg}} = \frac{1}{K} \sum_{k=1}^K \mathcal{D}_{W_2}^2(p(\hat{\mathbf{x}}_0^{\mathcal{F}} \mid \mathbf{y}_k^{\mathcal{F}}; \boldsymbol{\zeta}, \bar{\alpha}), p(\mathbf{x}_0^{\mathcal{F}} \mid \mathbf{y}_k^{\mathcal{F}})) \quad (15)$$

This formulation accommodates two regimes. For  $K = 1$ , the optimization is performed for a single realization of  $\mathbf{y}$ , reducing to the standard *Wasserstein-2* distance.

$$\begin{aligned} [\mathcal{D}_{W_2}^2]_{\text{Avg}} = & \sum_{i=1}^d \left( \sqrt{\lambda_i} - [\mathbf{D}_1]_i \right)^2 + \\ & \sum_{i=1}^d [\mathbf{D}_2 - \mathbf{A}]_i^2 [\mathbf{y}^{\mathcal{F}}]_i^2 + [\mathbf{D}_3 - \mathbf{I} + \mathbf{A} \mathbf{\Lambda}_H]_i^2 [\boldsymbol{\mu}_0^{\mathcal{F}}]_i^2 \end{aligned} \quad (16)$$

where:  $\mathbf{A} = \mathbf{\Lambda}_0 \mathbf{\Lambda}_{h^*} (\mathbf{\Lambda}_h \mathbf{\Lambda}_0 \mathbf{\Lambda}_{h^*} + \sigma_n^2 \mathbf{I})^{-1}$ .

Alternatively, when multiple realizations are considered, the weight parameters can be adjusted to capture the expected behavior of the posterior  $p(\mathbf{x}_0^{\mathcal{F}} \mid \mathbf{y}^{\mathcal{F}})$  across  $\mathbf{y}^{\mathcal{F}}$ , thereby eliminating the need to solve the optimization for each observation. In this setting, the optimal solution admits a closed-form expression in terms of the prior characteristics:

$$\begin{aligned} [\mathcal{D}_{W_2}^2]_{\text{Avg}} = & \sum_i^d \left( \sqrt{\lambda_0^{(i)}} - \mathbf{D}_1^{(i)} \right)^2 + \\ & \text{Tr}(\mathbf{M}^T \mathbf{M} (\mathbf{\Lambda}_h \mathbf{\Lambda}_0 \mathbf{\Lambda}_{h^*} + \sigma_n^2 \mathbf{I})) + \|\mathbf{M} \mathbf{\Lambda}_h \boldsymbol{\mu}_0^{\mathcal{F}} + \mathbf{b}\|_2^2 \end{aligned} \quad (17)$$

where  $\mathbf{M} = \mathbf{D}_2 - \mathbf{A}$  and  $\mathbf{b} = \mathbf{D}_3 - \mathbf{I} + \mathbf{A} \mathbf{\Lambda}_H$ , with  $\mathbf{D}_2$  and  $\mathbf{D}_3$  defined in (12). The full derivation is provided in Appendix E.

## 4. Optimal Gaussian Posterior Sampling

In this section, we formulate a closed-form expression for the posterior optimal denoiser under the Gaussian setting and analyze the reconstruction obtained when it is used within the diffusion process. The derived ideal posterior

<sup>1</sup>While  $\bar{\alpha}$  could be treated also as optimized argument, we focus on the current formulation.

sampler thus provides a principled reference for evaluating training-free posterior sampling methods and for assessing the effectiveness of our proposed recommendations under identical diffusion dynamics.

We adopt the notation introduced in Section 3.1. The clean signal  $\mathbf{x}_0 \in \mathbb{R}^d$  is modeled by a Gaussian prior,  $\mathbf{x}_0 \sim \mathcal{N}(\boldsymbol{\mu}_0, \boldsymbol{\Sigma}_0)$ . Observations  $\mathbf{y} \in \mathbb{R}^m$  follow  $\mathbf{y} = \mathbf{H}\mathbf{x}_0 + \mathbf{n}$  with a general linear operator  $\mathbf{H} \in \mathbb{R}^{m \times d}$  and  $\mathbf{n} \sim \mathcal{N}(\mathbf{0}, \sigma_y^2 \mathbf{I})$ . Under this modeling framework, the true posterior distribution  $p(\mathbf{x}_0|\mathbf{y})$  is also Gaussian,  $p(\mathbf{x}_0|\mathbf{y}) \sim \mathcal{N}(\boldsymbol{\mu}_{\mathbf{x}_0|\mathbf{y}}, \boldsymbol{\Sigma}_{\mathbf{x}_0|\mathbf{y}})$ , with the resulting expressions for the posterior mean and covariance provided in Appendix D.

#### 4.1. The Posterior Optimal Denoiser

We begin by deriving the exact optimal denoiser for the posterior. Under the Gaussian model described above, this denoiser coincides with both the posterior mean and the MAP estimator, and reduces to the classical Wiener filter in closed form. Such an ideal denoiser is tailored to a specific measurement operator  $\mathbf{H}$  and observation  $\mathbf{y}$ , and generally does not admit an analytic form beyond the Gaussian setting, necessitating approximations in practice.

**Theorem 4.1.** *Let  $\mathbf{x}_0 \sim \mathcal{N}(\boldsymbol{\mu}_0, \boldsymbol{\Sigma}_0)$  and let  $\mathbf{x}_t$  denote the noisy signal obtained from the forward diffusion process, as defined in (3). Given the linear measurement model  $\mathbf{y} = \mathbf{H}\mathbf{x}_0 + \mathbf{n}$ , the denoised signal obtained from the MAP estimator is given by:*

$$\mathbf{x}_0^* = \arg \max_{\mathbf{x}_0} \log p(\mathbf{x}_0|\mathbf{x}_t, \mathbf{y})$$

and admits the following closed-form:

$$\begin{aligned} \mathbf{x}_0^* = & \left( (1-\bar{\alpha}_t) \boldsymbol{\Sigma}_0 \mathbf{H}^T \mathbf{H} + \sigma_y^2 \bar{\alpha}_t \boldsymbol{\Sigma}_0 + \sigma_y^2 (1-\bar{\alpha}_t) \mathbf{I} \right)^{-1} \\ & \left( (1-\bar{\alpha}_t) \boldsymbol{\Sigma}_0 \mathbf{H}^T \mathbf{y} + \sigma_y^2 \sqrt{\bar{\alpha}_t} \boldsymbol{\Sigma}_0 \mathbf{x}_t + \sigma_y^2 (1-\bar{\alpha}_t) \boldsymbol{\mu}_0 \right) \end{aligned} \quad (18)$$

A detailed proof is given in Appendix A.

#### 4.2. Reverse Process Formulation

We now turn to describe the discrete sampling procedure, as introduced in (Ho et al., 2020; Song et al., 2021) instantiated using optimal denoiser derived in (18). In particular, we focus on the DDIM formulation (Song et al., 2021), as it facilitates an accelerated sampling framework.

**Lemma 4.2.** *Assume  $\mathbf{x}_0 \sim \mathcal{N}(\boldsymbol{\mu}_0, \boldsymbol{\Sigma}_0)$ , and let  $\bar{\alpha}$  be the noise schedule parameters. Given the linear measurement model  $\mathbf{y} = \mathbf{H}\mathbf{x}_0 + \mathbf{n}$ , the relation between two consecutive steps in the DDIM inference process, when using the posterior optimal denoiser in (18), is given by:*

$$\begin{aligned} \mathbf{x}_{s-1} = & (a_s + b_s \bar{\boldsymbol{\Sigma}}_{0,s}^{-1} \sigma_y^2 \sqrt{\bar{\alpha}_s} \boldsymbol{\Sigma}_0) \mathbf{x}_s \\ & + b_s \bar{\boldsymbol{\Sigma}}_{0,s}^{-1} (1 - \bar{\alpha}_s) (\boldsymbol{\Sigma}_0 \mathbf{H}^T \mathbf{y} + \sigma_y^2 \boldsymbol{\mu}_0) \end{aligned} \quad (19)$$

where:  $\bar{\boldsymbol{\Sigma}}_{0,s} = (1 - \bar{\alpha}_s) \boldsymbol{\Sigma}_0 \mathbf{H}^T \mathbf{H} + \sigma_y^2 \bar{\alpha}_s \boldsymbol{\Sigma}_0 + (1 - \bar{\alpha}_s) \sigma_y^2 \mathbf{I}$ , with  $a_s$  and  $b_s$  denoting diagonal matrices determined by the noise schedule  $\bar{\alpha}$ .

The derivation is provided in Appendix B.

#### 4.3. Migrating to spectral domain

Here, we adopt the assumptions and notation introduced in Section 3.3. By projecting both sides of Equation (19) onto the Fourier basis  $\mathbf{F}$  and recursively applying the update over  $S$  diffusion steps, we obtain the reconstructed output  $\hat{\mathbf{x}}_{0,opt}^{\mathcal{F}}$ , where the superscript  $\mathcal{F}$  denotes the Fourier-domain representation.

**Lemma 4.3.** *Assume  $\mathbf{x}_0 \sim \mathcal{N}(\boldsymbol{\mu}_0, \boldsymbol{\Sigma}_0)$ , and let  $\mathbf{y} = \mathbf{H}\mathbf{x}_0 + \mathbf{n}$  denote a linear measurement model. The frequency domain reconstruction obtained using DDIM with the optimal denoiser in (18) follows a Gaussian distribution and is given by:*

$$p(\hat{\mathbf{x}}_{0,opt}^{\mathcal{F}}|\mathbf{y}^{\mathcal{F}}) \sim \mathcal{N}(\mathbf{V}_2 \mathbf{y}^{\mathcal{F}} + \mathbf{V}_3 \boldsymbol{\mu}_0^{\mathcal{F}}, \mathbf{V}_1^2) \quad (20)$$

The matrices,  $\mathbf{V}_1$ ,  $\mathbf{V}_2$ , and  $\mathbf{V}_3$  are diagonal and depend on the noise schedule parameters  $\bar{\alpha}$  and on the prior distribution in the Fourier domain,  $\mathbf{x}_0^{\mathcal{F}} \sim \mathcal{N}(\boldsymbol{\mu}_0^{\mathcal{F}}, \boldsymbol{\Lambda}_0)$ .

For brevity, we only present the final result here; a full derivation is provided in Appendix C. Consequently, under the Gaussianity assumption, the ideal posterior sampler admits a closed-form expression that decouples into  $d$  independent scalar *transfer functions*. This formulation serves as principled reference for analyzing and interpreting existing posterior sampling methods.

## 5. Related work

Diffusion models have been widely used to address inverse problems in a training-free manner (Daras et al., 2024). One line of work incorporates measurements by enforcing data consistency through projection-based geometric operations, such as null-space decompositions and pseudoinverse operators (Choi et al., 2021; Wang et al., 2022; Kawar et al., 2022; Zhu et al., 2023). Another line adopts a Bayesian perspective, integrating measurement information through likelihood-based guidance (Bansal et al., 2023; Xu & Chi, 2024). Among these methods, DPS (Chung et al., 2022a) employs a point-estimate approximation of the clean signal motivated by Jensen’s inequality, while PIIGDM (Song et al., 2023) further introduces time-dependent variances.

Despite enabling effective posterior sampling without task-specific retraining, these approaches face practical challenges. In particular, they often require small guidance step sizes to maintain stability, thereby requiring a larger number of sampling steps and slowing inference (He et al.,

2023). To address this issue, DSG (Yang et al., 2024) introduces the notion of manifold deviation during sampling and proposes constraints that allow larger guidance step sizes. Similarly, DAPS (Zhang et al., 2025) employs an annealing strategy that decouples consecutive steps in the diffusion trajectory, improving stability at larger step sizes. Related works further explore how inference-time dynamics, such as manifold constraints or noise modulation, affect the tradeoff between perceptual quality and data fidelity in diffusion models (Chung et al., 2022b; He et al., 2023; Wang et al., 2025). Nevertheless, most training-free posterior sampling methods still rely on manual hyperparameter tuning, which directly affects both stability and performance.

Recently, the design of heuristics for diffusion models has been widely studied (Watson et al., 2021; Xia et al., 2023; Wang et al., 2023; Tong et al., 2024; Chen et al., 2024; Xue et al., 2024; Williams et al., 2024). In particular, Benita et al. (2025) proposed a spectral approach for determining the noise schedule in prior sampling. Using Gaussian modeling, they expressed the diffusion process as a transfer function and formulated an optimization problem for heuristic design. In the context of posterior sampling, Bellchambers (2025) addressed the purely denoising task using the prior score, and considered their solution transferable to related inverse problems. While their approach provided heuristic recommendations for DPS, it involved per-instance optimization during inference, which increased synthesis time.

## 6. Experiments

We turn to validate our approach through a series of experiments, examining our spectral recommendations compared to existing heuristics, and analyzing current sampling methods relative to the derived optimal posterior sampler.

### 6.1. Synthetic Gaussian distribution

In this section, we evaluate our approach considering a Gaussian prior distribution  $\mathbf{x}_0 \sim \mathcal{N}(\boldsymbol{\mu}_0, \boldsymbol{\Sigma}_0)$ , where  $\mathbf{x}_0 \in \mathbb{R}^d$  and  $\boldsymbol{\Sigma}_0 \in \mathbb{R}^{d \times d}$  is a circulant covariance matrix. Specifically, we define the prior covariance as  $\boldsymbol{\Sigma}_0 = A^T A$ , where  $A$  is a circulant matrix whose first row is given by  $a = [-l, -l + 1/(d-1), \dots, l - 1/(d-1), l]$ . The mean vector  $\boldsymbol{\mu}_0$  is chosen to be constant value vector, corresponding to a stationary model. In addition, the measurements  $\mathbf{y} \in \mathbb{R}^d$  are generated by a linear degradation model  $\mathbf{y} = \mathbf{H}\mathbf{x}_0 + \mathbf{n}$  with an operator  $\mathbf{H}$  and an additive Gaussian noise  $\mathbf{n} \sim \mathcal{N}(\mathbf{0}, \sigma_y^2 \mathbf{I})$ . In particular,  $\mathbf{H}$  acts as a low-pass filter (LPF), preserving a fraction  $\mathcal{V} \in (0, 1)$  of the frequency components. Under these settings,  $\boldsymbol{\Sigma}_0$  and  $\mathbf{H}$  commute and are diagonalized by the DFT. Accordingly, in the frequency domain, the prior covariance is represented by a diagonal matrix  $\boldsymbol{\Lambda}_0$  with eigenvalues  $\{\lambda_i\}_{i=1}^d$ , while the linear operator corresponds to a diagonal matrix  $\boldsymbol{\Lambda}_h$  with a

fraction of  $\mathcal{V}$  nonzero symmetric entries.

We begin by solving the optimization problem defined in (16) independently for each of  $N = 5$  observations  $\{\mathbf{y}^{(i)}\}_{i=1}^N$  using the DPS method and for different number diffusion steps. The index  $i$  denotes different realizations, each corresponding to an independently sampled signal  $\mathbf{x}_0^{(i)}$  and noise  $\mathbf{n}^{(i)}$ . We set  $\mathcal{V} = 0.5$  and  $\sigma_y = 0.1$ , and consider a prior with mean  $\boldsymbol{\mu}_0 = \mathbf{0}$  and a covariance of dimension  $d = 50$  parameterized by  $l = 0.05$ .

Figure (1) shows the resulting spectral recommendations for the weighting coefficients  $\boldsymbol{\zeta}$ , along with the mean and standard deviation across realizations. While the recommendations vary with the number of diffusion steps, their overall structure is preserved. Notably, higher weights are assigned at the early stages of the diffusion process and gradually decrease toward the end, with greater variability across realizations observed at the beginning of the process.

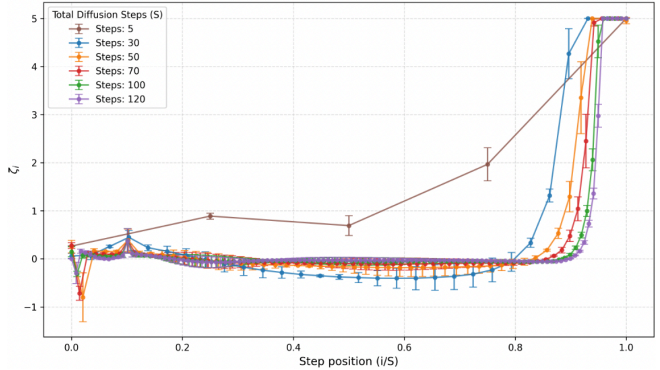


Figure 1. Spectral recommendations for the weighting coefficients  $\boldsymbol{\zeta}$  in DPS for different numbers of diffusion steps  $S \in [5, 30, 50, 70, 100, 120]$ , with variability across realizations.

Next, we compare our spectral recommendations with the weighting scheme used in DPS (Chung et al., 2022a) under the same experimental setting. Since these weights are chosen heuristically, we manually evaluate several values of  $\boldsymbol{\zeta}'$  to explore the effect of different heuristic choices. For each value, the experiment is repeated using the same realizations considered previously. Figure 2 provides a comparison for 70 diffusion steps. Interestingly, due to the inverse dependence of the DPS weights on the measurement error norm, their overall structure exhibits an opposing trend, with increasing values toward the end of the diffusion process.

The Gaussian setting allows direct evaluation of the posterior for a given observation  $\mathbf{y}_i$ , which is generally infeasible for non-Gaussian priors when only a single ground-truth sample  $\mathbf{x}_i$  is available. Leveraging this property, Figure 3 compares the Wasserstein-2 distance between reconstructed and true posterior distributions for several heuristic choices and the spectral recommendation across diffusion steps and realizations. In addition, we include the distance obtained for the analytically derived optimal posterior sampler (20).

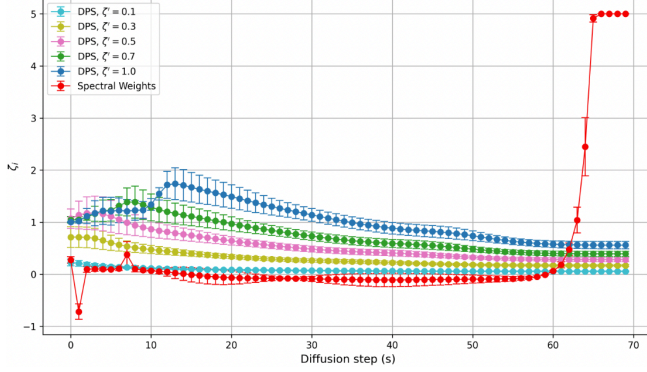


Figure 2. Comparison between the spectral recommendations (red) and DPS weighting coefficients for 70 diffusion steps, evaluated for different heuristic values of  $\zeta' \in \{0.1, 0.3, 0.5, 0.7, 1.0\}$ .

This exact solution serves as an idealized reference for evaluating the different methods and is generally unavailable in practice. While some heuristic choices outperform others, the spectral recommendation consistently achieves near-optimal performance across diffusion steps and exhibits greater stability across realizations. As expected, the ideal sampler yields the lowest Wasserstein distance overall.

Our approach is method-agnostic and can be applied to different posterior samplers. For brevity, Appendix H.1 shows the spectral recommendations derived for  $\Pi$ GDM and compare them to its heuristic counterpart using the Wasserstein-2 distance. Notably, the  $\Pi$ GDM heuristic weights depend only on the diffusion dynamics and decrease over diffusion steps, in contrast to DPS. For completeness, Figure 3 also includes the Wasserstein distance obtained for the  $\Pi$ GDM spectral recommendations. These distances are slightly lower than those for DPS, likely because the  $\Pi$ GDM likelihood approximation also incorporates an uncertainty term.

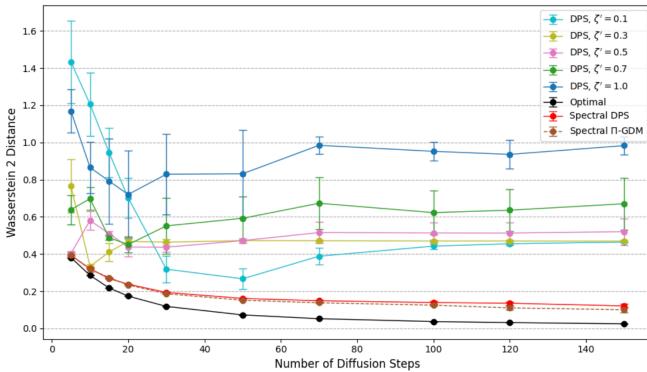


Figure 3. Comparison of the Wasserstein-2 distance for DPS heuristic values  $\zeta' \in \{0.1, 0.3, 0.5, 0.7, 1.0\}$ , the spectral recommendations applied to DPS (red) and to  $\Pi$ GDM (brown, dotted), and the analytically derived ideal posterior sampler (black), across different number of diffusion steps  $S \in \{5, 10, 15, 20, 30, 50, 70, 100, 120, 150\}$ .

Perceptual metrics such as the Wasserstein-2 distance may indicate high similarity between distributions and be asso-

ciated with visually realistic samples, while individual reconstructions can still deviate substantially from the ground-truth realization (Blau & Michaeli, 2018). Further comparisons on this aspect are provided in Section 6.2.

## 6.2. Empirical distribution

We now turn to evaluate our method on real-world datasets, FFHQ  $256 \times 256$  (Karras et al., 2019) and ImageNet  $256 \times 256$  (Deng et al., 2009), using the DPS framework. In order to derive the spectral recommendations, we fit a Gaussian distribution for each dataset by estimating its mean and covariance and then solve the optimization problem in (17). This approach incorporates the probabilistic properties of the degraded measurements, whereas the formulation in (16) is solved independently per observation and discussed separately. The estimation details are provided Appendix K.

Figure 4 shows the spectral weights obtained for the FFHQ dataset under LPF degradation with  $\mathcal{V} = 0.1$  and  $\sigma_y = 0.1$ , across different diffusion step counts. For comparison, we also include the weighting heuristics used by DPS, averaged over 100 syntheses, with variability indicated. Interestingly, the optimization reveals different weight structures with guidance values that increase over diffusion steps. While the DPS weights remain small, the spectral recommendations tend to place greater emphasis on the observations, suggesting a different balance between prior information and likelihood. Additional examples, including spectral recommendations for ImageNet, are provided in Appendix I.

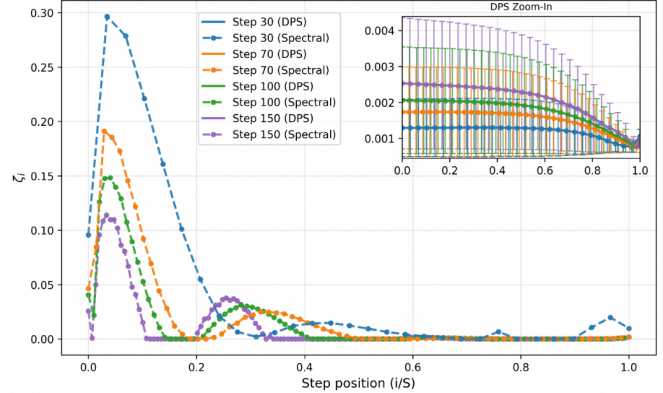


Figure 4. Comparison of spectral recommendations on the FFHQ dataset, with a zoomed-in view of the DPS heuristics. Results are shown for selected diffusion steps  $S \in \{30, 70, 100, 150\}$ .

We next examine the spectral recommendations during inference. Since the optimal prior denoiser is not available in practice, we used pretrained models from (Chung et al., 2022a) for both datasets, which introduces approximation error. To maintain consistency with the denoiser training, we employ the DDIM formulation with a linear noise schedule.

In our first experiment, we assess prior characteristics. We randomly select 1,000 images from the validation set, each

degraded independently and reconstructed once using the DPS framework with either the spectral recommendations or the DPS heuristic. For evaluation, we report peak signal-to-noise ratio (PSNR), structural similarity index measure (SSIM) (Wang et al., 2004), Learned Perceptual Image Patch Similarity (LPIPS) (Zhang et al., 2018), and Fréchet Inception Distance (FID) (Heusel et al., 2017), all computed using the piq library (Kastrulyin et al., 2022), with images normalized to the  $[0, 1]$  range.

Table 1 reports the results on the FFHQ dataset across different number of diffusion steps. Overall, our recommendations achieve a more balanced tradeoff between measurement fidelity and perceptual quality compared to the DPS heuristic. At relatively smaller numbers of diffusion steps, DPS heuristic attains lower FID values; however, qualitative results in Appendix I, suggest that this behavior is associated with its small likelihood weights, leading the samples to be dominated by the pretrained prior. While this can enhance perceptual appearance, the resulting images may deviate from the observed measurements, which is undesirable in inverse problems. Additional comparisons and further analysis across different  $\mathcal{V}$  and  $\sigma_y$  values, including ImageNet results, are provided in Appendix I, where similar conclusions are observed.

Table 1. Quantitative evaluation on FFHQ, comparing spectral recommendations with DPS heuristics ( $\mathcal{V}=0.1$  and  $\sigma_y=0.1$ ).

METHOD	STEPS	PSNR↑	SSIM↑	LPIPS↓	FID↓
DPS	100	14.06	0.35	0.63	<b>120.52</b>
	200	16.65	0.43	0.55	<b>97.04</b>
	300	18.11	0.47	0.51	87.79
	400	19.18	0.50	0.49	82.26
SPECTRAL	100	<b>16.87</b>	<b>0.49</b>	<b>0.58</b>	130.05
	200	<b>17.89</b>	<b>0.51</b>	<b>0.53</b>	107.91
	300	<b>21.37</b>	<b>0.59</b>	<b>0.45</b>	<b>79.2</b>
	400	<b>22.35</b>	<b>0.61</b>	<b>0.42</b>	<b>68.3</b>

We proceed with an analysis of the posterior behavior under fixed observations. To this end, we select three representative images and apply the same degradation as in the first experiment. We consider both optimization formulations introduced in Section 3.4. The first, given in (17), captures expected posterior behavior across degraded measurements and is solved once for a fixed degradation operator. The second, defined in (16), is solved independently for each observation and yields realization-specific recommendations.

For each image, we generate 1,000 reconstructions across different numbers of diffusion steps and compute the corresponding performance metrics. Unlike the prior analysis, which averages over images, this experiment fixes the observation and probes the posterior through multiple reconstructions per image. The results, summarized in Table 2, indicate that both spectral optimization strategies generally

offer a balance between measurement fidelity and sample naturalness, with the realization-specific approach providing a modest but consistent improvement by adapting to individual observations. This benefit, however, comes at the cost of solving a separate optimization problem for each realization. Qualitative results and further details are provided in Appendix J.

Table 2. Mean quantitative results for the posterior sampling on FFHQ 256, comparing DPS heuristics with spectral parameter recommendations from the expected and realization-specific optimizations. Results are averaged across three realizations.

METHOD	STEPS	PSNR↑	SSIM↑	LPIPS↓
DPS	100	14.99	0.35	0.61
	200	18.15	0.44	<b>0.52</b>
	300	19.88	0.49	0.48
	400	21.04	0.53	0.45
SPECTRAL	100	<u>17.55</u>	<u>0.51</u>	<b>0.56</b>
	200	<u>19.01</u>	<u>0.53</u>	<b>0.52</b>
	300	<u>23.05</u>	<u>0.62</u>	<b>0.43</b>
	400	<u>23.47</u>	<u>0.61</u>	0.42
SPECTRAL $K=1$	100	<b>18.48</b>	<b>0.53</b>	0.53
	200	<b>22.24</b>	<b>0.59</b>	0.44
	300	<b>23.08</b>	<u>0.62</u>	<b>0.41</b>
	400	<b>24.76</b>	<b>0.63</b>	<b>0.39</b>

Since optimization times may vary in settings involving high-resolution images or a large number of diffusion steps, we adopt the acceleration strategies proposed in (Benita et al., 2025). Specifically, we employ iterative initialization, where solutions obtained for smaller numbers of inference steps is used to initialize the optimization at larger number of steps, and dimensionality reduction via PCA, which projects the problem onto the dominant prior directions. Details on the resulting solution times are provided in Appendix L.

## 7. Conclusion

In this work, we propose a spectral approach for analyzing zero-shot diffusion posterior sampling methods. Under a Gaussian assumption, we derive the output distributions induced by these samplers as well as the ideal posterior sampler, which provides a theoretical reference for analysis. We demonstrate how our approach enables a principled design of the heuristic components used by these schemes, while jointly accounting for properties of the prior, the degraded observations, and the dynamics of the diffusion process. Finally, we examine our recommendation on existing methods and characterize their behavior in terms of sample naturalness and measurement fidelity. We hope this work offers a useful perspective to inform future research on developing and analyzing zero-shot posterior sampling methods.

## Impact Statement

This paper presents work whose goal is to advance the field of Machine Learning. There are many potential societal consequences of our work, none which we feel must be specifically highlighted here.

## References

Arjovsky, M., Chintala, S., and Bottou, L. Wasserstein generative adversarial networks. In *International conference on machine learning*, pp. 214–223. PMLR, 2017.

Bansal, A., Chu, H.-M., Schwarzschild, A., Sengupta, S., Goldblum, M., Geiping, J., and Goldstein, T. Universal guidance for diffusion models. In *Proceedings of the IEEE/CVF conference on computer vision and pattern recognition*, pp. 843–852, 2023.

Bellchambers, G. Exploiting the exact denoising posterior score in training-free guidance of diffusion models. *arXiv preprint arXiv:2506.13614*, 2025.

Benita, R., Elad, M., and Keshet, J. Spectral analysis of diffusion models with application to schedule design. *arXiv preprint arXiv:2502.00180*, 2025.

Blau, Y. and Michaeli, T. The perception-distortion trade-off. In *Proceedings of the IEEE conference on computer vision and pattern recognition*, pp. 6228–6237, 2018.

Chen, D., Zhou, Z., Wang, C., Shen, C., and Lyu, S. On the trajectory regularity of ode-based diffusion sampling. *arXiv preprint arXiv:2405.11326*, 2024.

Choi, J., Kim, S., Jeong, Y., Gwon, Y., and Yoon, S. Ilvr: Conditioning method for denoising diffusion probabilistic models. *arXiv preprint arXiv:2108.02938*, 2021.

Chung, H., Kim, J., Mccann, M. T., Klasky, M. L., and Ye, J. C. Diffusion posterior sampling for general noisy inverse problems. *arXiv preprint arXiv:2209.14687*, 2022a.

Chung, H., Sim, B., Ryu, D., and Ye, J. C. Improving diffusion models for inverse problems using manifold constraints. *Advances in Neural Information Processing Systems*, 35:25683–25696, 2022b.

Daras, G., Chung, H., Lai, C.-H., Mitsufuji, Y., Ye, J. C., Milanfar, P., Dimakis, A. G., and Delbracio, M. A survey on diffusion models for inverse problems. *arXiv preprint arXiv:2410.00083*, 2024.

Deng, J., Dong, W., Socher, R., Li, L.-J., Li, K., and Fei-Fei, L. Imagenet: A large-scale hierarchical image database. In *Proceedings of the IEEE Conference on Computer Vision and Pattern Recognition*, 2009.

Dong, C., Loy, C. C., He, K., and Tang, X. Image super-resolution using deep convolutional networks. *IEEE transactions on pattern analysis and machine intelligence*, 38(2):295–307, 2015.

Efron, B. Tweedie’s formula and selection bias. *Journal of the American Statistical Association*, 106(496):1602–1614, 2011.

Freirich, D., Michaeli, T., and Meir, R. A theory of the distortion-perception tradeoff in wasserstein space. *Advances in Neural Information Processing Systems*, 34: 25661–25672, 2021.

He, Y., Murata, N., Lai, C.-H., Takida, Y., Uesaka, T., Kim, D., Liao, W.-H., Mitsufuji, Y., Kolter, J. Z., Salakhutdinov, R., et al. Manifold preserving guided diffusion. *arXiv preprint arXiv:2311.16424*, 2023.

Heusel, M., Ramsauer, H., Unterthiner, T., Nessler, B., and Hochreiter, S. Gans trained by a two time-scale update rule converge to a local nash equilibrium. *Advances in neural information processing systems*, 30, 2017.

Ho, J., Jain, A., and Abbeel, P. Denoising diffusion probabilistic models. *Advances in neural information processing systems*, 33:6840–6851, 2020.

Karras, T., Laine, S., and Aila, T. A style-based generator architecture for generative adversarial networks. In *Proceedings of the IEEE/CVF Conference on Computer Vision and Pattern Recognition*, 2019.

Kastryulin, S., Zakirov, J., Prokopenko, D., and Dylov, D. V. Pytorch image quality: Metrics for image quality assessment. *arXiv preprint arXiv:2208.14818*, 2022.

Kawar, B., Elad, M., Ermon, S., and Song, J. Denoising diffusion restoration models. *Advances in neural information processing systems*, 35:23593–23606, 2022.

Kullback, S. and Leibler, R. A. On information and sufficiency. *The annals of mathematical statistics*, 22(1): 79–86, 1951.

Saharia, C., Chan, W., Chang, H., Lee, C., Ho, J., Salimans, T., Fleet, D., and Norouzi, M. Palette: Image-to-image diffusion models. In *ACM SIGGRAPH 2022 conference proceedings*, pp. 1–10, 2022.

Song, J., Meng, C., and Ermon, S. Denoising diffusion implicit models. In *International Conference on Learning Representations (ICLR)*, 2021.

Song, J., Vahdat, A., Mardani, M., and Kautz, J. Pseudoinverse-guided diffusion models for inverse problems. In *International Conference on Learning Representations*, 2023.

Song, Y., Sohl-Dickstein, J., Kingma, D. P., Kumar, A., Ermon, S., and Poole, B. Score-based generative modeling through stochastic differential equations. *arXiv preprint arXiv:2011.13456*, 2020.

Tong, V., Trung-Dung, H., Liu, A., Broeck, G. V. d., and Niepert, M. Learning to discretize denoising diffusion odes. *arXiv preprint arXiv:2405.15506*, 2024.

Unser, M. On the approximation of the discrete karhunen-loeve transform for stationary processes. *Signal Processing*, 7(3):231–249, 1984.

Wang, Y., Yu, J., and Zhang, J. Zero-shot image restoration using denoising diffusion null-space model. *arXiv preprint arXiv:2212.00490*, 2022.

Wang, Y., Wang, X., Dinh, A.-D., Du, B., and Xu, C. Learning to schedule in diffusion probabilistic models. In *Proceedings of the 29th ACM SIGKDD Conference on Knowledge Discovery and Data Mining*, pp. 2478–2488, 2023.

Wang, Y., Bi, S., Zhang, Y.-J. A., and Yuan, X. Traversing distortion-perception tradeoff using a single score-based generative model. In *Proceedings of the Computer Vision and Pattern Recognition Conference*, pp. 2377–2386, 2025.

Wang, Z., Bovik, A. C., Sheikh, H. R., and Simoncelli, E. P. Image quality assessment: from error visibility to structural similarity. *IEEE transactions on image processing*, 13(4):600–612, 2004.

Watson, D., Chan, W., Ho, J., and Norouzi, M. Learning fast samplers for diffusion models by differentiating through sample quality. In *International Conference on Learning Representations*, 2021.

Williams, C., Campbell, A., Doucet, A., and Syed, S. Score-optimal diffusion schedules. *Advances in Neural Information Processing Systems*, 37:107960–107983, 2024.

Xia, M., Shen, Y., Lei, C., Zhou, Y., Yi, R., Zhao, D., Wang, W., and Liu, Y.-j. Towards more accurate diffusion model acceleration with a timestep aligner. *arXiv preprint arXiv:2310.09469*, 2023.

Xu, X. and Chi, Y. Provably robust score-based diffusion posterior sampling for plug-and-play image reconstruction. *Advances in Neural Information Processing Systems*, 37:36148–36184, 2024.

Xue, S., Liu, Z., Chen, F., Zhang, S., Hu, T., Xie, E., and Li, Z. Accelerating diffusion sampling with optimized time steps. In *Proceedings of the IEEE/CVF Conference on Computer Vision and Pattern Recognition*, pp. 8292–8301, 2024.

Yang, L., Ding, S., Cai, Y., Yu, J., Wang, J., and Shi, Y. Guidance with spherical gaussian constraint for conditional diffusion. *arXiv preprint arXiv:2402.03201*, 2024.

Yu, J., Wang, Y., Zhao, C., Ghanem, B., and Zhang, J. Freedom: Training-free energy-guided conditional diffusion model. In *Proceedings of the IEEE/CVF International Conference on Computer Vision*, pp. 23174–23184, 2023.

Zhang, B., Chu, W., Berner, J., Meng, C., Anandkumar, A., and Song, Y. Improving diffusion inverse problem solving with decoupled noise annealing. In *Proceedings of the Computer Vision and Pattern Recognition Conference*, pp. 20895–20905, 2025.

Zhang, R., Isola, P., and Efros, A. A. Colorful image colorization. In *European conference on computer vision*, pp. 649–666. Springer, 2016.

Zhang, R., Isola, P., Efros, A. A., Shechtman, E., and Wang, O. The unreasonable effectiveness of deep features as a perceptual metric. In *Proceedings of the IEEE conference on computer vision and pattern recognition*, pp. 586–595, 2018.

Zhu, Y., Zhang, K., Liang, J., Cao, J., Wen, B., Timofte, R., and Van Gool, L. Denoising diffusion models for plug-and-play image restoration. In *Proceedings of the IEEE/CVF conference on computer vision and pattern recognition*, pp. 1219–1229, 2023.

## A. The Optimal Denoiser for a Gaussian Posterior

Let  $\mathbf{x}_0 \sim \mathcal{N}(\boldsymbol{\mu}_0, \boldsymbol{\Sigma}_0)$  represent the distribution of the original dataset, where  $\mathbf{x}_0 \in \mathbb{R}^d$ . A general linear inverse problem is posed as:  $\mathbf{y} = \mathbf{H}\mathbf{x}_0 + \mathbf{n}$  with  $\mathbf{y} \in \mathbb{R}^m$ ,  $\mathbf{H} \in \mathbb{R}^{m \times d}$  a known linear degradation matrix, and  $\mathbf{n} \sim \mathcal{N}(\mathbf{0}, \sigma_y^2 \mathbf{I})$  i.i.d. additive Gaussian noise with known variance.

Under the Gaussian prior and linear measurement model, the posterior distribution of  $\mathbf{x}_0$  given  $\mathbf{y}$  is Gaussian; consequently, the MAP estimator coincides with the posterior mean and takes the form of a Wiener filter, which is optimal under mean-squared error.

For the Maximum A Posteriori (MAP) estimation, we seek to maximize the posterior distribution:

$$\max_{\mathbf{x}_0} \log p(\mathbf{x}_0 | \mathbf{x}_t, \mathbf{y})$$

Using Bayes' rule, this can be written as:

$$\begin{aligned} \min_{\mathbf{x}_0} -\log \left[ \frac{p(\mathbf{y} | \mathbf{x}_0, \mathbf{x}_t) p(\mathbf{x}_0 | \mathbf{x}_t)}{p(\mathbf{y} | \mathbf{x}_t)} \right] \\ \min_{\mathbf{x}_0} -\log p(\mathbf{y} | \mathbf{x}_0, \mathbf{x}_t) - \log p(\mathbf{x}_0 | \mathbf{x}_t) \end{aligned} \quad (21)$$

Since  $\mathbf{y}$  is conditionally independent of  $\mathbf{x}_t$  given  $\mathbf{x}_0$ , The conditional log-likelihood  $\log p(\mathbf{y} | \mathbf{x}_0, \mathbf{x}_t)$  is given by:

$$\begin{aligned} p(\mathbf{y} | \mathbf{x}_0, \mathbf{x}_t) &= \mathcal{N}(\mathbf{y}; \mathbf{H}\mathbf{x}_0, \sigma_y^2 \mathbf{I}) = \frac{1}{\sqrt{(2\pi\sigma_y^2)^d}} \exp \left\{ -\frac{1}{2\sigma_y^2} (\mathbf{y} - \mathbf{H}\mathbf{x}_0)^T (\mathbf{y} - \mathbf{H}\mathbf{x}_0) \right\} \\ \log p(\mathbf{y} | \mathbf{x}_0, \mathbf{x}_t) &= -\frac{1}{2} \log (2\pi\sigma_y^2)^d - \frac{1}{2\sigma_y^2} (\mathbf{y} - \mathbf{H}\mathbf{x}_0)^T (\mathbf{y} - \mathbf{H}\mathbf{x}_0) \end{aligned} \quad (22)$$

Using Bayes' rule,  $\log p(\mathbf{x}_0 | \mathbf{x}_t) \propto \log p(\mathbf{x}_t | \mathbf{x}_0) + \log p(\mathbf{x}_0)$

Through the diffusion process, the signal undergoes noise contamination, leading to the following marginal expression for  $\mathbf{x}_t$ :

$$\mathbf{x}_t = \sqrt{\bar{\alpha}_t} \mathbf{x}_0 + \sqrt{1 - \bar{\alpha}_t} \boldsymbol{\epsilon} \quad \boldsymbol{\epsilon} \sim \mathcal{N}(\mathbf{0}, \mathbf{I}) \quad (23)$$

where  $\alpha_t$  for  $t \in [1, T]$  is referred to as the incremental noise schedule and  $\bar{\alpha}_t = \prod_{i=1}^t \alpha_i$ .

Hence, the conditional log-likelihood  $\log p(\mathbf{x}_t | \mathbf{x}_0)$  is given by:

$$\begin{aligned} p(\mathbf{x}_t | \mathbf{x}_0) &= \mathcal{N}(\mathbf{x}_t; \sqrt{\bar{\alpha}_t} \mathbf{x}_0, (1 - \bar{\alpha}_t) \mathbf{I}) = \frac{1}{\sqrt{(2\pi(1 - \bar{\alpha}_t))^d}} \exp \left\{ -\frac{1}{2(1 - \bar{\alpha}_t)} (\mathbf{x}_t - \sqrt{\bar{\alpha}_t} \mathbf{x}_0)^T (\mathbf{x}_t - \sqrt{\bar{\alpha}_t} \mathbf{x}_0) \right\} \\ \log p(\mathbf{x}_t | \mathbf{x}_0) &= -\frac{1}{2} \log (2\pi(1 - \bar{\alpha}_t))^d - \frac{1}{2(1 - \bar{\alpha}_t)} (\mathbf{x}_t - \sqrt{\bar{\alpha}_t} \mathbf{x}_0)^T (\mathbf{x}_t - \sqrt{\bar{\alpha}_t} \mathbf{x}_0) \end{aligned} \quad (24)$$

The log-likelihood  $\log p(\mathbf{x}_0)$  is given by:

$$p(\mathbf{x}_0) = \mathcal{N}(\mathbf{x}_0; \boldsymbol{\mu}, \boldsymbol{\Sigma}_0) = \frac{1}{\sqrt{(2\pi)^d |\boldsymbol{\Sigma}_0|}} \exp \left\{ -\frac{1}{2} (\mathbf{x}_0 - \boldsymbol{\mu}_0)^T \boldsymbol{\Sigma}_0^{-1} (\mathbf{x}_0 - \boldsymbol{\mu}_0) \right\} \quad (25)$$

$$\log p(\mathbf{x}_0) = -\frac{1}{2} \log (2\pi)^d |\boldsymbol{\Sigma}_0| - \frac{1}{2} (\mathbf{x}_0 - \boldsymbol{\mu}_0)^T \boldsymbol{\Sigma}_0^{-1} (\mathbf{x}_0 - \boldsymbol{\mu}_0) \quad (26)$$

By substituting the expressions from Equations 22, 24, and 25 into Equation 21 and differentiating with respect to  $\mathbf{x}_0$ , we obtain:

$$-\frac{2\mathbf{H}^T(\mathbf{y} - \mathbf{H}\mathbf{x}_0)}{2\sigma_y^2} - \frac{2\sqrt{\bar{\alpha}_t}(\mathbf{x}_t - \sqrt{\bar{\alpha}_t}\mathbf{x}_0)}{2(1 - \bar{\alpha}_t)} + \frac{2\boldsymbol{\Sigma}_0^{-1}(\mathbf{x}_0 - \boldsymbol{\mu}_0)}{2} = 0$$

This simplifies to:

$$-\frac{\mathbf{H}^T(\mathbf{y} - \mathbf{H}\mathbf{x}_0)}{\sigma_y^2} - \frac{\sqrt{\bar{\alpha}_t}(\mathbf{x}_t - \sqrt{\bar{\alpha}_t}\mathbf{x}_0)}{(1 - \bar{\alpha}_t)} + \boldsymbol{\Sigma}_0^{-1}(\mathbf{x}_0 - \boldsymbol{\mu}_0) = 0$$

Resulting in:

$$-(1 - \bar{\alpha}_t)\boldsymbol{\Sigma}_0\mathbf{H}^T(\mathbf{y} - \mathbf{H}\mathbf{x}_0) - \sigma_y^2\sqrt{\bar{\alpha}_t}\boldsymbol{\Sigma}_0(\mathbf{x}_t - \sqrt{\bar{\alpha}_t}\mathbf{x}_0) + \sigma_y^2(1 - \bar{\alpha}_t)(\mathbf{x}_0 - \boldsymbol{\mu}_0) = 0$$

Thus:

$$((1 - \bar{\alpha}_t)\boldsymbol{\Sigma}_0\mathbf{H}^T\mathbf{H} + \sigma_y^2\bar{\alpha}_t\boldsymbol{\Sigma}_0 + I\sigma_y^2(1 - \bar{\alpha}_t))\mathbf{x}_0 = (1 - \bar{\alpha}_t)\boldsymbol{\Sigma}_0\mathbf{H}^T\mathbf{y} + \sigma_y^2\sqrt{\bar{\alpha}_t}\boldsymbol{\Sigma}_0\mathbf{x}_t + \sigma_y^2(1 - \bar{\alpha}_t)\boldsymbol{\mu}_0$$

Finally:

$$\begin{aligned} \mathbf{x}_0^* &= ((1 - \bar{\alpha}_t)\boldsymbol{\Sigma}_0\mathbf{H}^T\mathbf{H} + \sigma_y^2\bar{\alpha}_t\boldsymbol{\Sigma}_0 + I\sigma_y^2(1 - \bar{\alpha}_t))^{-1} \\ &\quad ((1 - \bar{\alpha}_t)\boldsymbol{\Sigma}_0\mathbf{H}^T\mathbf{y} + \sigma_y^2\sqrt{\bar{\alpha}_t}\boldsymbol{\Sigma}_0\mathbf{x}_t + \sigma_y^2(1 - \bar{\alpha}_t)\boldsymbol{\mu}_0) \end{aligned} \quad (27)$$

## B. The Reverse Process in the Time Domain

Here, we present the reverse process in the time domain for the DDIM (Song et al., 2021). Let  $\mathbf{x}_0$  follow the distribution:

$$\mathbf{x}_0 \sim \mathcal{N}(\boldsymbol{\mu}_0, \boldsymbol{\Sigma}_0), \quad \mathbf{x}_0 \in \mathbb{R}^d$$

Using the procedure outline in (Song et al., 2021), the diffusion process begins with  $\mathbf{x}_S \sim \mathcal{N}(\mathbf{0}, \mathbf{I})$ , where  $\mathbf{x}_S \in \mathbb{R}^d$  and progresses through an iterative denoising process described as follows:<sup>2</sup>

$$\mathbf{x}_{s-1}(\eta) = \sqrt{\bar{\alpha}_{s-1}} \left( \frac{\mathbf{x}_s - \sqrt{1 - \bar{\alpha}_s} \cdot \boldsymbol{\epsilon}_\theta(\mathbf{x}_s, s)}{\sqrt{\bar{\alpha}_s}} \right) + \sqrt{1 - \bar{\alpha}_{s-1} - \sigma_s^2(\eta)} \cdot \boldsymbol{\epsilon}_\theta(\mathbf{x}_s, s) + \sigma_s(\eta) \mathbf{z}_s \quad (28)$$

where

$$\sigma_s(\eta) = \eta \sqrt{\frac{1 - \bar{\alpha}_{s-1}}{1 - \bar{\alpha}_s}} \sqrt{1 - \frac{\bar{\alpha}_s}{\bar{\alpha}_{s-1}}} \quad (29)$$

Substituting the marginal property from (3):

$$\boldsymbol{\epsilon}_\theta(\mathbf{x}_s, s) = \frac{\mathbf{x}_s - \sqrt{\bar{\alpha}_s}\hat{\mathbf{x}}_0}{\sqrt{1 - \bar{\alpha}_s}} \quad \hat{\mathbf{x}}_0 = \frac{\mathbf{x}_s - \sqrt{1 - \bar{\alpha}_s} \cdot \boldsymbol{\epsilon}_\theta(\mathbf{x}_s, s)}{\sqrt{\bar{\alpha}_s}} \quad (30)$$

$$\mathbf{x}_{s-1}(\eta) = \sqrt{\bar{\alpha}_{s-1}}\hat{\mathbf{x}}_0 + \sqrt{1 - \bar{\alpha}_{s-1} - \sigma_s^2(\eta)} \left( \frac{\mathbf{x}_s - \sqrt{\bar{\alpha}_s}\hat{\mathbf{x}}_0}{\sqrt{1 - \bar{\alpha}_s}} \right) + \sigma_s(\eta) \mathbf{z}_s \quad (31)$$

<sup>2</sup>We follow here the DDIM notations that replaces  $t$  with  $s$ , where the steps  $[1, \dots, S]$  form a subsequence of  $[1, \dots, T]$  and  $S = T$ .

For the deterministic scenario, we choose  $\eta = 0$  in (29) and obtain  $\sigma_s(\eta = 0) = 0$ . Therefore:

$$\begin{aligned}\mathbf{x}_{s-1}(\eta = 0) &= \sqrt{\bar{\alpha}_{s-1}}\hat{\mathbf{x}}_0 + \sqrt{1 - \bar{\alpha}_{s-1}} \left( \frac{\mathbf{x}_s - \sqrt{\bar{\alpha}_s}\hat{\mathbf{x}}_0}{\sqrt{1 - \bar{\alpha}_s}} \right) \\ &= \frac{\sqrt{1 - \bar{\alpha}_{s-1}}}{\sqrt{1 - \bar{\alpha}_s}} \mathbf{x}_s + \left[ \sqrt{\bar{\alpha}_{s-1}} - \frac{\sqrt{\bar{\alpha}_s}\sqrt{1 - \bar{\alpha}_{s-1}}}{\sqrt{1 - \bar{\alpha}_s}} \right] \hat{\mathbf{x}}_0\end{aligned}\quad (32)$$

We define:

$$a_s = \left[ \frac{\sqrt{1 - \bar{\alpha}_{s-1}}}{\sqrt{1 - \bar{\alpha}_s}} \right] \mathbf{I} \quad b_s = \left[ \sqrt{\bar{\alpha}_{s-1}} - \frac{\sqrt{\bar{\alpha}_s}\sqrt{1 - \bar{\alpha}_{s-1}}}{\sqrt{1 - \bar{\alpha}_s}} \right] \mathbf{I}$$

Therefore, the update can be written as:

$$\mathbf{x}_{s-1} = a_s \mathbf{x}_s + b_s \mathbf{x}_0^*.$$

Substituting the MAP estimator from Equation 27 into the DDIM update yields

$$\begin{aligned}\mathbf{x}_{s-1} &= a_s \mathbf{x}_s + \\ &b_s \left[ \left( (1 - \bar{\alpha}_s) \mathbf{\Sigma}_0 \mathbf{H}^T \mathbf{H} + \sigma_y^2 \bar{\alpha}_s \mathbf{\Sigma}_0 + \mathbf{I} \sigma_y^2 (1 - \bar{\alpha}_s) \right)^{-1} \left( (1 - \bar{\alpha}_s) \mathbf{\Sigma}_0 \mathbf{H}^T \mathbf{y} + \sigma_y^2 \sqrt{\bar{\alpha}_s} \mathbf{\Sigma}_0 \mathbf{x}_s + \sigma_y^2 (1 - \bar{\alpha}_s) \boldsymbol{\mu}_0 \right) \right] \\ \mathbf{x}_{s-1} &= \left[ a_s + b_s \left[ \left( (1 - \bar{\alpha}_s) \mathbf{\Sigma}_0 \mathbf{H}^T \mathbf{H} + \sigma_y^2 \bar{\alpha}_s \mathbf{\Sigma}_0 + \mathbf{I} \sigma_y^2 (1 - \bar{\alpha}_s) \right)^{-1} \right] \sigma_y^2 \sqrt{\bar{\alpha}_s} \mathbf{\Sigma}_0 \right] \mathbf{x}_s + \\ &b_s \left( (1 - \bar{\alpha}_s) \mathbf{\Sigma}_0 \mathbf{H}^T \mathbf{H} + \sigma_y^2 \bar{\alpha}_s \mathbf{\Sigma}_0 + \mathbf{I} \sigma_y^2 (1 - \bar{\alpha}_s) \right)^{-1} \left( (1 - \bar{\alpha}_s) \mathbf{\Sigma}_0 \mathbf{H}^T \mathbf{y} \right) + \\ &b_s \left( (1 - \bar{\alpha}_s) \mathbf{\Sigma}_0 \mathbf{H}^T \mathbf{H} + \sigma_y^2 \bar{\alpha}_s \mathbf{\Sigma}_0 + \mathbf{I} \sigma_y^2 (1 - \bar{\alpha}_s) \right)^{-1} \left( \sigma_y^2 (1 - \bar{\alpha}_s) \boldsymbol{\mu}_0 \right)\end{aligned}$$

We define:

$$\bar{\mathbf{\Sigma}}_{0,s} = (1 - \bar{\alpha}_s) \mathbf{\Sigma}_0 \mathbf{H}^T \mathbf{H} + \sigma_y^2 \bar{\alpha}_s \mathbf{\Sigma}_0 + \mathbf{I} \sigma_y^2 (1 - \bar{\alpha}_s)$$

Using this notation, the update becomes:

$$\begin{aligned}\mathbf{x}_{s-1} &= \left( a_s + b_s (\bar{\mathbf{\Sigma}}_{0,s})^{-1} \sigma_y^2 \sqrt{\bar{\alpha}_s} \mathbf{\Sigma}_0 \right) \mathbf{x}_s + b_s (\bar{\mathbf{\Sigma}}_{0,s})^{-1} \left( (1 - \bar{\alpha}_s) \mathbf{\Sigma}_0 \mathbf{H}^T \mathbf{y} \right) \\ &+ b_s (\bar{\mathbf{\Sigma}}_{0,s})^{-1} \left( \sigma_y^2 (1 - \bar{\alpha}_s) \boldsymbol{\mu}_0 \right)\end{aligned}\quad (33)$$

## C. Migrating to the Spectral Domain

To migrate to the spectral domain, we apply the Discrete Fourier Transform (DFT), represented by the unitary matrix  $\mathbf{F}$ , to both sides of the DDIM update:

$$\begin{aligned}\mathbf{x}_{s-1}^{\mathcal{F}} &= \mathbf{F} \left( a_s + b_s \bar{\mathbf{\Sigma}}_{0,s}^{-1} \sigma_y^2 \sqrt{\bar{\alpha}_s} \mathbf{\Sigma}_0 \right) \mathbf{x}_s \mathbf{F}^T \\ &+ \mathbf{F} b_s \bar{\mathbf{\Sigma}}_{0,s}^{-1} \left( (1 - \bar{\alpha}_s) \mathbf{\Sigma}_0 \mathbf{H}^T \mathbf{y} + \sigma_y^2 (1 - \bar{\alpha}_s) \boldsymbol{\mu}_0 \right) \mathbf{F}^T,\end{aligned}\quad (34)$$

where the superscript  $\mathcal{F}$  indicates the Fourier-domain representation of a vector, e.g.,  $\mathbf{x}_s^{\mathcal{F}} = \mathbf{F} \mathbf{x}_s$ .

$$\begin{aligned}\mathbf{x}_{s-1}^{\mathcal{F}} &= a_s \mathbf{x}_s^{\mathcal{F}} + \mathbf{F} b_s (\bar{\mathbf{\Sigma}}_{0,s})^{-1} \mathbf{F}^T \mathbf{F} \sigma_y^2 \sqrt{\bar{\alpha}_s} \mathbf{\Sigma}_0 \mathbf{F}^T \mathbf{F} \mathbf{x}_s \\ &+ b_s \mathbf{F} (\bar{\mathbf{\Sigma}}_{0,s})^{-1} \mathbf{F}^T \mathbf{F} (1 - \bar{\alpha}_s) \mathbf{\Sigma}_0 \mathbf{F}^T \mathbf{F} \mathbf{H}^T \mathbf{F}^T \mathbf{F} \mathbf{y} + b_s \mathbf{F} (\bar{\mathbf{\Sigma}}_{0,s})^{-1} \mathbf{F}^T \mathbf{F} \sigma_y^2 (1 - \bar{\alpha}_s) \boldsymbol{\mu}_0\end{aligned}\quad (35)$$

$$\begin{aligned}\mathbf{x}_{s-1}^{\mathcal{F}} &= a_s \mathbf{x}_s^{\mathcal{F}} + b_s \mathbf{F} (\bar{\Sigma}_{0,s})^{-1} \mathbf{F}^T \sqrt{\bar{\alpha}_s} \sigma_y^2 \mathbf{F} \Sigma_0 \mathbf{F}^T \mathbf{x}_s^{\mathcal{F}} \\ &+ b_s \mathbf{F} (\bar{\Sigma}_{0,s})^{-1} \mathbf{F}^T (1 - \bar{\alpha}_s) (\mathbf{F} \Sigma_0 \mathbf{F}^T) (\mathbf{F} \mathbf{H}^T \mathbf{F}^T) \mathbf{y}^{\mathcal{F}} + b_s \mathbf{F} (\bar{\Sigma}_{0,s})^{-1} \mathbf{F}^T \sigma_y^2 (1 - \bar{\alpha}_s) \boldsymbol{\mu}_0^{\mathcal{F}}\end{aligned}\quad (36)$$

Assuming that  $\mathbf{H}$  is circulant with eigenvalues  $\{h_i\}_{i=1}^d$ , and noting that  $\Sigma_0$  is also circulant, both matrices commute and can be diagonalized via the Discrete Fourier Transform (DFT) matrix  $\mathbf{F}$ , which greatly simplifies the matrix inversion. Specifically:

- $\Lambda_0 = \mathbf{F} \Sigma_0 \mathbf{F}^T, \quad \Sigma_0 = \mathbf{F}^T \Lambda_0 \mathbf{F}$
- $\mathbf{H} = \mathbf{F}^T \Lambda_{\mathbf{H}} \mathbf{F}, \quad \mathbf{H}^T = \mathbf{F}^T \Lambda_{\mathbf{H}^T} \mathbf{F}, \quad \mathbf{H}^T \mathbf{H} = \mathbf{F}^T \Lambda_{\mathbf{H}^T \mathbf{H}} \mathbf{F}$
- $a \Sigma_0 + b \mathbf{I} = a \mathbf{F} \Lambda_0 \mathbf{F}^T + b \mathbf{F} \mathbf{I} \mathbf{F}^T = \mathbf{F} (a \Lambda_0 + b \mathbf{I}) \mathbf{F}^T$
- $\Sigma_0^{-1} = \mathbf{F} \Lambda_0^{-1} \mathbf{F}^T, \quad \Lambda_0^{-1} = \mathbf{F}^T \Sigma_0^{-1} \mathbf{F}$

Therefore, we obtain:

$$\Sigma_0 \mathbf{H}^T \mathbf{H} = \mathbf{F}^T \Lambda_0 \mathbf{F} \mathbf{F}^T \Lambda_{\mathbf{H}^T \mathbf{H}} \mathbf{F} = \mathbf{F}^T \Lambda_0 \Lambda_{\mathbf{H}^T \mathbf{H}} \mathbf{F}$$

and:

$$\begin{aligned}\mathbf{F} (\bar{\Sigma}_{0,s})^{-1} \mathbf{F}^T &= \mathbf{F} [(1 - \bar{\alpha}_s) \Sigma_0 \mathbf{H}^T \mathbf{H} + \sigma_y^2 \bar{\alpha}_s \Sigma_0 + \sigma_y^2 (1 - \bar{\alpha}_s) \mathbf{I}]^{-1} \mathbf{F}^T \\ &= ((1 - \bar{\alpha}_s) \Lambda_0 \Lambda_{\mathbf{H}^T \mathbf{H}} + \sigma_y^2 \bar{\alpha}_s \Lambda_0 + \sigma_y^2 (1 - \bar{\alpha}_s) \mathbf{I})^{-1} \\ &= \text{diag} ((1 - \bar{\alpha}_s) \lambda_i h_i^2 + \sigma_y^2 \bar{\alpha}_s \lambda_i + \sigma_y^2 (1 - \bar{\alpha}_s) \mathbf{I})^{-1}\end{aligned}$$

$$\mathbf{F} (\bar{\Sigma}_{0,s})^{-1} \mathbf{F}^T = \text{diag} \left( \frac{1}{(1 - \bar{\alpha}_s) \lambda_i h_i^2 + \sigma_y^2 \bar{\alpha}_s \lambda_i + \sigma_y^2 (1 - \bar{\alpha}_s)} \right)$$

We denote the expression as:

$$\mathbf{F} (\bar{\Sigma}_{0,s})^{-1} \mathbf{F}^T = \text{diag} \left( \frac{1}{\lambda_{sum}} \right) = \Lambda_{sum}^{-1} \quad (37)$$

Substitute 37 into 36

$$\mathbf{x}_{s-1}^{\mathcal{F}} = a_s \mathbf{x}_s^{\mathcal{F}} + b_s \Lambda_{sum}^{-1} \sqrt{\bar{\alpha}_s} \sigma_y^2 \Lambda_0 \mathbf{x}_s^{\mathcal{F}} + b_s \Lambda_{sum}^{-1} (1 - \bar{\alpha}_s) \Lambda_0 \Lambda_{\mathbf{H}^T} \mathbf{y}^{\mathcal{F}} + b_s \Lambda_{sum}^{-1} \sigma_y^2 (1 - \bar{\alpha}_s) \boldsymbol{\mu}_0^{\mathcal{F}}$$

$$\mathbf{x}_{s-1}^{\mathcal{F}} = [a_s + b_s \Lambda_{sum}^{-1} \sqrt{\bar{\alpha}_s} \sigma_y^2 \Lambda_0] \mathbf{x}_s^{\mathcal{F}} + b_s \Lambda_{sum}^{-1} (1 - \bar{\alpha}_s) \Lambda_0 \Lambda_{\mathbf{H}^T} \mathbf{y}^{\mathcal{F}} + b_s \sigma_y^2 (1 - \bar{\alpha}_s) \Lambda_{sum}^{-1} \boldsymbol{\mu}_0^{\mathcal{F}}$$

We can then recursively obtain  $\mathbf{x}_m^{\mathcal{F}}$  for a general  $m$ :

$$\mathbf{x}_m^{\mathcal{F}} = \prod_{s=m+1}^S [a_s + b_s \Lambda_{sum}^{-1} \sqrt{\bar{\alpha}_s} \sigma_y^2 \Lambda_0] \mathbf{x}_s^{\mathcal{F}} + \left[ \sum_{i=m+1}^S [b_i \Lambda_{sum}^{-1} (1 - \bar{\alpha}_s) \Lambda_0 \Lambda_{\mathbf{H}^T}] \prod_{j=m+1}^{i-1} [a_j + b_j \Lambda_{sum}^{-1} \sqrt{\bar{\alpha}_s} \sigma_y^2 \Lambda_0] \right] \mathbf{y}^{\mathcal{F}}$$

$$+ \left[ \sum_{i=m+1}^S [b_i \sigma_y^2 (1 - \bar{\alpha}_s) \boldsymbol{\Lambda}_{sum}^{-1}] \prod_{j=m+1}^{i-1} [a_j + b_j \boldsymbol{\Lambda}_{sum}^{-1} \sqrt{\bar{\alpha}_s} \sigma_y^2 \boldsymbol{\Lambda}_0] \right] \boldsymbol{\mu}_0^{\mathcal{F}}$$

specifically for  $m=0$ :

$$\begin{aligned} \mathbf{x}_0^{\mathcal{F}} &= \prod_{s=1}^S [a_s + b_s \boldsymbol{\Lambda}_{sum}^{-1} \sqrt{\bar{\alpha}_s} \sigma_y^2 \boldsymbol{\Lambda}_0] \mathbf{x}_S^{\mathcal{F}} + \left[ \sum_{i=1}^S [b_i \boldsymbol{\Lambda}_{sum}^{-1} (1 - \bar{\alpha}_s) \boldsymbol{\Lambda}_0 \boldsymbol{\Lambda}_{\mathbf{H}^T}] \prod_{j=1}^{i-1} [a_j + b_j \boldsymbol{\Lambda}_{sum}^{-1} \sqrt{\bar{\alpha}_s} \sigma_y^2 \boldsymbol{\Lambda}_0] \right] \mathbf{y}^{\mathcal{F}} \\ &+ \left[ \sum_{i=1}^S [b_i \sigma_y^2 (1 - \bar{\alpha}_s) \boldsymbol{\Lambda}_{sum}^{-1}] \prod_{j=1}^{i-1} [a_j + b_j \boldsymbol{\Lambda}_{sum}^{-1} \sqrt{\bar{\alpha}_s} \sigma_y^2 \boldsymbol{\Lambda}_0] \right] \boldsymbol{\mu}_0^{\mathcal{F}} \end{aligned}$$

we will denote the following:

$$\begin{aligned} \mathbf{V}_1 &= \prod_{s=1}^S [a_s + b_s \boldsymbol{\Lambda}_{sum}^{-1} \sqrt{\bar{\alpha}_s} \sigma_y^2 \boldsymbol{\Lambda}_0] \mathbf{x}_S^{\mathcal{F}} \\ \mathbf{V}_2 &= \left[ \sum_{i=1}^S [b_i \boldsymbol{\Lambda}_{sum}^{-1} (1 - \bar{\alpha}_s) \boldsymbol{\Lambda}_0 \boldsymbol{\Lambda}_{\mathbf{H}^T}] \prod_{j=1}^{i-1} [a_j + b_j \boldsymbol{\Lambda}_{sum}^{-1} \sqrt{\bar{\alpha}_s} \sigma_y^2 \boldsymbol{\Lambda}_0] \right] \\ \mathbf{V}_3 &= \left[ \sum_{i=1}^S [b_i \sigma_y^2 (1 - \bar{\alpha}_s) \boldsymbol{\Lambda}_{sum}^{-1}] \prod_{j=1}^{i-1} [a_j + b_j \boldsymbol{\Lambda}_{sum}^{-1} \sqrt{\bar{\alpha}_s} \sigma_y^2 \boldsymbol{\Lambda}_0] \right] \end{aligned}$$

$$\mathbf{x}_0^{\mathcal{F}} = \mathbf{V}_1 \mathbf{x}_S^{\mathcal{F}} + \mathbf{V}_2 \mathbf{y}^{\mathcal{F}} + \mathbf{V}_3 \boldsymbol{\mu}_0^{\mathcal{F}} \quad (38)$$

Given the closed-form expression for  $\mathbf{x}_0^{\mathcal{F}}$  in Equation 38, we derive its mean and covariance as functions of the problem settings.

**Mean:**

$$\begin{aligned} \boldsymbol{\mu}_{opt} &= \mathbb{E} [\mathbf{V}_1 \mathbf{x}_S^{\mathcal{F}} + \mathbf{V}_2 \mathbf{y}^{\mathcal{F}} + \mathbf{V}_3 \boldsymbol{\mu}_0^{\mathcal{F}} \mid \mathbf{y}] = \mathbf{V}_1 \mathbf{F} \mathbb{E} [\mathbf{x}_S \mid \mathbf{y}] + \mathbf{V}_2 \mathbf{F} \mathbb{E} [\mathbf{y} \mid \mathbf{y}] + \mathbf{V}_3 \mathbf{F} \mathbb{E} [\boldsymbol{\mu}_0 \mid \mathbf{y}] \\ &= \mathbf{V}_1 \mathbf{F} \mathbb{E} [\mathbf{x}_S] + \mathbf{V}_2 \mathbf{F} \mathbf{y} + \mathbf{V}_3 \mathbf{F} \boldsymbol{\mu}_0 \\ &= \mathbf{V}_2 \mathbf{y}^{\mathcal{F}} + \mathbf{V}_3 \boldsymbol{\mu}_0^{\mathcal{F}} \end{aligned}$$

$$\boxed{\boldsymbol{\mu}_{opt} = \mathbb{E} [\mathbf{V}_1 \mathbf{x}_S^{\mathcal{F}} + \mathbf{V}_2 \mathbf{y}^{\mathcal{F}} + \mathbf{V}_3 \boldsymbol{\mu}_0^{\mathcal{F}}] = \mathbf{V}_2 \mathbf{y}^{\mathcal{F}} + \mathbf{V}_3 \boldsymbol{\mu}_0^{\mathcal{F}}} \quad (39)$$

**Covariance:**

$$\begin{aligned}
 \Lambda_{opt} &= \mathbb{E}[(\mathbf{V}_1 \mathbf{x}_S^{\mathcal{F}} + \mathbf{V}_2 \mathbf{y}^{\mathcal{F}} + \mathbf{V}_3 \boldsymbol{\mu}_0^{\mathcal{F}} - \mathbb{E}[\mathbf{V}_1 \mathbf{x}_S^{\mathcal{F}} + \mathbf{V}_2 \mathbf{y}^{\mathcal{F}} + \mathbf{V}_3 \boldsymbol{\mu}_0^{\mathcal{F}} | \mathbf{y}]) \\
 &\quad (\mathbf{V}_1 \mathbf{x}_S^{\mathcal{F}} + \mathbf{V}_2 \mathbf{y}^{\mathcal{F}} + \mathbf{V}_3 \boldsymbol{\mu}_0^{\mathcal{F}} - \mathbb{E}[\mathbf{V}_1 \mathbf{x}_S^{\mathcal{F}} + \mathbf{V}_2 \mathbf{y}^{\mathcal{F}} + \mathbf{V}_3 \boldsymbol{\mu}_0^{\mathcal{F}} | \mathbf{y}])^T | \mathbf{y}] \\
 &= \mathbb{E}[(\mathbf{V}_1 \mathbf{x}_S^{\mathcal{F}} + \mathbf{V}_2 \mathbf{y}^{\mathcal{F}} + \mathbf{V}_3 \boldsymbol{\mu}_0^{\mathcal{F}} - \mathbf{V}_2 \mathbf{y}^{\mathcal{F}} - \mathbf{V}_3 \boldsymbol{\mu}_0^{\mathcal{F}})(\mathbf{V}_1 \mathbf{x}_S^{\mathcal{F}} + \mathbf{V}_2 \mathbf{y}^{\mathcal{F}} + \mathbf{V}_3 \boldsymbol{\mu}_0^{\mathcal{F}} - \mathbf{V}_2 \mathbf{y}^{\mathcal{F}} - \mathbf{V}_3 \boldsymbol{\mu}_0^{\mathcal{F}})^T | \mathbf{y}] \\
 &= \mathbb{E}[(\mathbf{V}_1 \mathbf{x}_S^{\mathcal{F}})(\mathbf{V}_1 \mathbf{x}_S^{\mathcal{F}})^T | \mathbf{y}] \\
 &= \mathbf{V}_1 \mathbb{E}[\mathbf{x}_S^{\mathcal{F}} (\mathbf{x}_S^{\mathcal{F}})^T] \mathbf{V}_1^T \\
 &= \mathbf{V}_1 \mathbf{V}_1^T
 \end{aligned}$$

$$\boxed{\Lambda_{opt} = \mathbf{V}_1^2} \quad (40)$$

## D. Gaussian Posterior Distribution

Here, we derive a closed-form expression for  $p(\mathbf{x} | \mathbf{y})$  under a linear degradation model. Specifically, we assume that the clean signal  $\mathbf{x} \sim \mathcal{N}(\boldsymbol{\mu}_0, \boldsymbol{\Sigma}_0)$  and the noise  $\mathbf{n} \sim \mathcal{N}(\mathbf{0}, \sigma_n^2 \mathbf{I})$  are independent Gaussian vectors, and that the observation is given by a linear transformation  $\mathbf{y} = \mathbf{Hx} + \mathbf{n}$ , where  $\mathbf{H}$  is a deterministic matrix. Under these assumptions, the joint distribution  $p(\mathbf{x}, \mathbf{y})$  is Gaussian.

Define the concatenated vector  $\mathbf{z} = \begin{pmatrix} \mathbf{x} \\ \mathbf{y} \end{pmatrix} = \begin{pmatrix} \mathbf{x} \\ \mathbf{Hx} + \mathbf{n} \end{pmatrix}$ . Then  $\mathbf{z}$  is jointly Gaussian with mean and covariance:

$$\mathbb{E}[\mathbf{z}] = \boldsymbol{\mu}_{(x,y)} = \begin{pmatrix} \boldsymbol{\mu}_x \\ \boldsymbol{\mu}_y \end{pmatrix}, \quad \boldsymbol{\Sigma}_{\mathbf{z}} = \boldsymbol{\Sigma}_{(x,y)} = \begin{pmatrix} \boldsymbol{\Sigma}_x & \boldsymbol{\Sigma}_{xy} \\ \boldsymbol{\Sigma}_{yx} & \boldsymbol{\Sigma}_y \end{pmatrix}$$

where:

$$\begin{aligned}
 \boldsymbol{\mu}_x &= \boldsymbol{\mu}_0 \\
 \boldsymbol{\mu}_y &= \mathbb{E}[\mathbf{y}] = \mathbb{E}[\mathbf{Hx} + \mathbf{n}] = \mathbf{H}\mathbb{E}[\mathbf{x}] + \mathbb{E}[\mathbf{n}] = \mathbf{H}\boldsymbol{\mu}_0
 \end{aligned}$$

The covariance of  $\mathbf{y}$  is then simply

$$\boldsymbol{\Sigma}_y = \text{Cov}[\mathbf{y}] = \mathbf{H}\boldsymbol{\Sigma}_x\mathbf{H}^T + \sigma_n^2 \mathbf{I},$$

Hence:

$$\boxed{p(\mathbf{y}) = \mathcal{N}(\mathbf{y}; \mathbf{H}\boldsymbol{\mu}_0, \mathbf{H}\boldsymbol{\Sigma}_x\mathbf{H}^T + \sigma_n^2 \mathbf{I})} \quad (41)$$

The cross-covariance is then:

$$\boldsymbol{\Sigma}_{xy} = \mathbb{E}[(\mathbf{x} - \boldsymbol{\mu}_x)(\mathbf{y} - \boldsymbol{\mu}_y)^T]$$

$$\boldsymbol{\Sigma}_{xy} = \text{Cov}[\mathbf{x}, \mathbf{y}] = \boldsymbol{\Sigma}_x \mathbf{H}^T, \quad \boldsymbol{\Sigma}_{yx} = \text{Cov}[\mathbf{y}, \mathbf{x}] = \mathbf{H} \boldsymbol{\Sigma}_x.$$

Therefore, we can derive the Joint Mean and Covariance of  $p(\mathbf{x}, \mathbf{y})$ :

$$\boldsymbol{\mu}_{(x,y)} = \begin{pmatrix} \boldsymbol{\mu}_0 \\ \mathbf{H}\boldsymbol{\mu}_x \end{pmatrix}, \quad \boldsymbol{\Sigma}_{(x,y)} = \begin{pmatrix} \boldsymbol{\Sigma}_x & \boldsymbol{\Sigma}_0 \mathbf{H}^T \\ \mathbf{H}^T \boldsymbol{\Sigma}_0 & \mathbf{H} \boldsymbol{\Sigma}_x \mathbf{H}^T + \sigma_n^2 \mathbf{I} \end{pmatrix}$$

To compute  $p(\mathbf{x} | \mathbf{y})$ , we use the standard result for joint Gaussian distributions: the conditional distribution is also Gaussian with mean and covariance:

**Mean of  $p(\mathbf{x} \mid \mathbf{y})$ :**

$$\begin{aligned}\boldsymbol{\mu}_{x|y} &= \boldsymbol{\mu}_x + \boldsymbol{\Sigma}_{xy} \boldsymbol{\Sigma}_y^{-1} (\mathbf{y} - \boldsymbol{\mu}_y) \\ &= \boldsymbol{\mu}_0 + \boldsymbol{\Sigma}_0 \mathbf{H}^T (\mathbf{H} \boldsymbol{\Sigma}_0 \mathbf{H}^T + \sigma_n^2 \mathbf{I})^{-1} (\mathbf{y} - \mathbf{H} \boldsymbol{\mu}_0)\end{aligned}\quad (42)$$

**Covariance of  $p(\mathbf{x} \mid \mathbf{y})$ :**

$$\begin{aligned}\boldsymbol{\Sigma}_{x|y} &= \boldsymbol{\Sigma}_x - \boldsymbol{\Sigma}_{xy} \boldsymbol{\Sigma}_y^{-1} \boldsymbol{\Sigma}_{yx} \\ &= \boldsymbol{\Sigma}_0 - \boldsymbol{\Sigma}_0 \mathbf{H}^T (\mathbf{H} \boldsymbol{\Sigma}_0 \mathbf{H}^T + \sigma_n^2 \mathbf{I})^{-1} \mathbf{H} \boldsymbol{\Sigma}_0\end{aligned}\quad (43)$$

Therefore, the conditional probability distribution  $p(x \mid y)$  is:

$$\boxed{p(\mathbf{x} \mid \mathbf{y}) = \mathcal{N}(\mathbf{x}; \boldsymbol{\mu}_0 + \boldsymbol{\Sigma}_0 \mathbf{H}^T (\mathbf{H} \boldsymbol{\Sigma}_0 \mathbf{H}^T + \sigma_n^2 \mathbf{I})^{-1} (\mathbf{y} - \mathbf{H} \boldsymbol{\mu}_0), \boldsymbol{\Sigma}_0 - \boldsymbol{\Sigma}_0 \mathbf{H}^T (\mathbf{H} \boldsymbol{\Sigma}_0 \mathbf{H}^T + \sigma_n^2 \mathbf{I})^{-1} \mathbf{H} \boldsymbol{\Sigma}_0)}$$

**Migrating to the spectral domain:**

Here we describe the posterior  $p(\mathbf{x} \mid \mathbf{y})$  in the spectral domain. Let  $\mathbf{F}$  denote the unitary Discrete Fourier Transform (DFT) matrix and the superscript  $\mathcal{F}$  denotes the Fourier-domain representation. Then

$$\begin{aligned}\boldsymbol{\mu}_{\mathbf{x}_0|\mathbf{y}}^{\mathcal{F}} &= \mathbf{F} \mathbb{E} [\mathbf{x}_0 \mid \mathbf{y}] \\ &= \mathbf{F} [\boldsymbol{\mu}_0 + \boldsymbol{\Sigma}_0 \mathbf{H}^T (\mathbf{H} \boldsymbol{\Sigma}_0 \mathbf{H}^T + \sigma_n^2 \mathbf{I})^{-1} (\mathbf{y} - \mathbf{H} \boldsymbol{\mu}_0)] \\ &= \mathbf{F} \boldsymbol{\mu}_0 + \mathbf{F} \boldsymbol{\Sigma}_0 \mathbf{F}^T \mathbf{F} \mathbf{H}^T \mathbf{F}^T \mathbf{F} (\mathbf{H} \boldsymbol{\Sigma}_{\mathbf{x}_0} \mathbf{H}^T + \sigma_n^2 \mathbf{I})^{-1} \mathbf{F}^T \mathbf{F} (\mathbf{y} - \mathbf{H} \boldsymbol{\mu}_0) \\ &= \boldsymbol{\mu}_0^{\mathcal{F}} + \boldsymbol{\Lambda}_0 \boldsymbol{\Lambda}_{H^T} (\boldsymbol{\Lambda}_H \boldsymbol{\Lambda}_0 \boldsymbol{\Lambda}_{H^T} - \boldsymbol{\Lambda}_H \boldsymbol{\mu}_0^{\mathcal{F}} \{ \boldsymbol{\mu}_0^{\mathcal{F}} \}^T \boldsymbol{\Lambda}_{H^T} + \sigma_n^2 \mathbf{I})^{-1} (\mathbf{y}^{\mathcal{F}} - \boldsymbol{\Lambda}_H \boldsymbol{\mu}_0^{\mathcal{F}})\end{aligned}$$

By defining:

$$\mathbf{H} = \mathbf{F}^T \boldsymbol{\Lambda}_H \mathbf{F}, \quad \mathbf{H}^T = \mathbf{F}^T \boldsymbol{\Lambda}_{H^T} \mathbf{F}, \quad \mathbf{H}^T \mathbf{H} = \mathbf{F}^T \boldsymbol{\Lambda}_{H^T} \mathbf{H} \mathbf{F}$$

and:

$$\mathbf{F} [\mathbf{H} \boldsymbol{\Sigma}_0 \mathbf{H}^T] \mathbf{F}^T = \mathbf{F} \mathbf{H} \mathbf{F}^T \mathbf{F} \boldsymbol{\Sigma}_0 \mathbf{F}^T \mathbf{F} \mathbf{H}^T \mathbf{F}^T = \boldsymbol{\Lambda}_H \boldsymbol{\Lambda}_0 \boldsymbol{\Lambda}_{H^T}$$

We get:

$$\boxed{\boldsymbol{\mu}_{\mathbf{x}_0|\mathbf{y}}^{\mathcal{F}} = \boldsymbol{\mu}_0^{\mathcal{F}} + \boldsymbol{\Lambda}_0 \boldsymbol{\Lambda}_{H^T} (\boldsymbol{\Lambda}_H \boldsymbol{\Lambda}_0 \boldsymbol{\Lambda}_{H^T} + \sigma_n^2 \mathbf{I})^{-1} (\mathbf{y}^{\mathcal{F}} - \boldsymbol{\Lambda}_H \boldsymbol{\mu}_0^{\mathcal{F}})} \quad (44)$$

$$\begin{aligned}\boldsymbol{\Lambda}_{x_0|y} &= \mathbf{F} \boldsymbol{\Sigma}_{\mathbf{x}_0|\mathbf{y}} \mathbf{F}^T \\ &= \mathbf{F} [\boldsymbol{\Sigma}_0 - \boldsymbol{\Sigma}_0 \mathbf{H}^T (\mathbf{H} \boldsymbol{\Sigma}_0 \mathbf{H}^T + \sigma_n^2 \mathbf{I})^{-1} \mathbf{H} \boldsymbol{\Sigma}_0] \mathbf{F}^T \\ &= \mathbf{F} \boldsymbol{\Sigma}_0 \mathbf{F}^T - \mathbf{F} \boldsymbol{\Sigma}_0 \mathbf{F}^T \mathbf{F} \mathbf{H}^T \mathbf{F}^T \mathbf{F} (\mathbf{H} \boldsymbol{\Sigma}_0 \mathbf{H}^T + \sigma_n^2 \mathbf{I})^{-1} \mathbf{F}^T \mathbf{F} \mathbf{H} \mathbf{F}^T \mathbf{F} \boldsymbol{\Sigma}_0 \mathbf{F}^T \\ &= \boldsymbol{\Lambda}_0 - \boldsymbol{\Lambda}_0 \boldsymbol{\Lambda}_{H^T} (\boldsymbol{\Lambda}_H \boldsymbol{\Lambda}_0 \boldsymbol{\Lambda}_{H^T} + \sigma_n^2 \mathbf{I})^{-1} \boldsymbol{\Lambda}_H \boldsymbol{\Lambda}_0\end{aligned}$$

Therefore:

$$\boxed{\boldsymbol{\Lambda}_{x_0|y} = \boldsymbol{\Lambda}_0 - \boldsymbol{\Lambda}_0 \boldsymbol{\Lambda}_{H^T} (\boldsymbol{\Lambda}_H \boldsymbol{\Lambda}_0 \boldsymbol{\Lambda}_{H^T} + \sigma_n^2 \mathbf{I})^{-1} \boldsymbol{\Lambda}_H \boldsymbol{\Lambda}_0} \quad (45)$$

## E. Averaged Wasserstein Distance

To bridge the analytical spectral recommendations with practical implementation, we formulate the optimization in terms of an average loss over the distribution of observations  $\mathbf{y}$ , modeled as  $\mathbf{y} \sim \mathcal{N}(\boldsymbol{\mu}_y, \boldsymbol{\Sigma}_y)$  with  $\mathbf{y} = \mathbf{H}\mathbf{x} + \mathbf{n}$ . We adopt the Average Wasserstein distance between the original and estimated posterior distributions as the loss function.

This formulation naturally accommodates two regimes. For a single observation ( $K = 1$ ), the optimization reduces to the standard Wasserstein-2 loss associated with that realization. Alternatively, when multiple realizations are considered, the weight parameters are optimized to capture the expected behavior of the posterior  $p(\mathbf{x} | \mathbf{y})$  across  $\mathbf{y}$ , eliminating the need to solve the optimization individually for each sample. In this average setting, the optimal solution can be expressed directly in terms of the statistical properties of  $p(\mathbf{y})$  rather than for a specific observation. In what follows, we derive the resulting average loss formulation for both the single-sample case ( $K = 1$ ) and the regime of large  $K$ .

The Wasserstein-2 distance between two Gaussian distributions with means  $\boldsymbol{\mu}_1$  and  $\boldsymbol{\mu}_2$ , and covariance matrices  $\boldsymbol{\Sigma}_1$  and  $\boldsymbol{\Sigma}_2$ , and the corresponding eigenvalues  $\{\lambda_1^{(i)}\}_{i=1}^d$  and  $\{\lambda_2^{(i)}\}_{i=1}^d$  is given by:

$$W_2(\mathcal{N}_1, \mathcal{N}_2) = \sqrt{(\boldsymbol{\mu}_1 - \boldsymbol{\mu}_2)^T(\boldsymbol{\mu}_1 - \boldsymbol{\mu}_2) + \sum_i \left( \sqrt{\lambda_1^{(i)}} - \sqrt{\lambda_2^{(i)}} \right)^2} \quad (46)$$

In addition, We define the average Wasserstein distance as:

$$[\mathcal{L}_{W_2}^2]_{\text{Avg}} = \frac{1}{K} \sum_{k=1}^K W_2^2(p(\mathbf{x}_0^{\mathcal{F}} | \mathbf{y}), p(\hat{\mathbf{x}}_0^{\mathcal{F}} | \mathbf{y}^{\mathcal{F}})) \quad (47)$$

Using the true posterior distribution derived in Section D and, for concreteness, the DPS posterior from Equation (65), we have

$$\hat{\mathbf{x}}_0^{\mathcal{F}} | \mathbf{y}^{\mathcal{F}} \sim \mathcal{N}(\mathbf{D}_2 \mathbf{y}^{\mathcal{F}} + \mathbf{D}_3 \boldsymbol{\mu}_0^{\mathcal{F}}, \mathbf{D}_1^2), \quad \hat{\mathbf{x}}_0^{\mathcal{F}} \in \mathbb{R}^d \quad \text{and} \quad \mathbf{x}_0^{\mathcal{F}} | \mathbf{y} \sim \mathcal{N}(\boldsymbol{\mu}_{\mathbf{x}_0 | \mathbf{y}}^{\mathcal{F}}, \boldsymbol{\Lambda}_{x_0 | y}), \quad \mathbf{x}_0^{\mathcal{F}} \in \mathbb{R}^d$$

Substituting these expressions into the Wasserstein formula yields:

$$[\mathcal{L}_{W_2}^2]_{\text{Avg}} = \frac{1}{K} \sum_{k=1}^K \left( \sum_i \left( \sqrt{\lambda_0^{(i)}} - \mathbf{D}_1^{(i)} \right)^2 + \sum_i \left( \boldsymbol{\mu}_{\mathbf{x}^{\mathcal{F}} | \mathbf{y}, k}^{(i)} - \boldsymbol{\mu}_{\hat{\mathbf{x}}^{\mathcal{F}} | \mathbf{y}, k}^{(i)} \right)^2 \right) \quad (48)$$

Where  $\{\lambda_0^{(i)}\}_{i=1}^d$  are the eigenvalues of  $p(\mathbf{x}_0^{\mathcal{F}} | \mathbf{y})$  located on the diagonal of the matrix  $\boldsymbol{\Lambda}_{x_0 | y}$  and  $\mathbf{D}_1^{(i)}$  denotes the  $i$ th diagonal entry of the matrix  $\mathbf{D}_1$ .

While for  $K = 1$  the average Wasserstein distance trivially reduces to the standard Wasserstein distance, we consider here the regime of large  $K$ . The mean of the true posterior from 44 can be written as:

$$\boldsymbol{\mu}_{\mathbf{x}^{\mathcal{F}} | \mathbf{y}} = \boldsymbol{\mu}_0^{\mathcal{F}} + \mathbf{A}(\mathbf{y}^{\mathcal{F}} - \boldsymbol{\Lambda}_H \boldsymbol{\mu}_0^{\mathcal{F}}) = \mathbf{A}\mathbf{y}^{\mathcal{F}} + (\mathbf{I} - \mathbf{A}\boldsymbol{\Lambda}_H) \boldsymbol{\mu}_0^{\mathcal{F}}$$

where:

$$\mathbf{A} = \boldsymbol{\Lambda}_0 \boldsymbol{\Lambda}_{H^T} (\boldsymbol{\Lambda}_H \boldsymbol{\Lambda}_0 \boldsymbol{\Lambda}_{H^T} + \sigma_n^2 \mathbf{I})^{-1}$$

Similarly, denoting the mean of the DPS posterior term using 65, we have

$$\boldsymbol{\mu}_{\hat{\mathbf{x}}^{\mathcal{F}} | \mathbf{y}} = \mathbf{D}_2 \mathbf{y}^{\mathcal{F}} + \mathbf{D}_3 \boldsymbol{\mu}_0^{\mathcal{F}}$$

Defining the mean discrepancy, we obtain:

$$\Delta\boldsymbol{\mu}(\mathbf{y}) = \boldsymbol{\mu}_{\hat{\mathbf{x}}^{\mathcal{F}} | \mathbf{y}} - \boldsymbol{\mu}_{\mathbf{x}^{\mathcal{F}} | \mathbf{y}} = (\mathbf{D}_2 - \mathbf{A}) \mathbf{y}^{\mathcal{F}} + (\mathbf{D}_3 - \mathbf{I} + \mathbf{A}\boldsymbol{\Lambda}_H) \boldsymbol{\mu}_0^{\mathcal{F}}$$

$$\Delta\boldsymbol{\mu}(\mathbf{y}) = \mathbf{M}\mathbf{y}^{\mathcal{F}} + \mathbf{b}$$

Focusing on the mean term of the Wasserstein-2 loss, we obtain the following compact quadratic form:

$$\begin{aligned}
 & \frac{1}{K} \sum_{k=1}^K \|\boldsymbol{\mu}_{\mathbf{x}^{\mathcal{F}}|\mathbf{y},k} - \boldsymbol{\mu}_{\hat{\mathbf{x}}^{\mathcal{F}}|\mathbf{y},k}\|_2^2 \\
 &= \frac{1}{K} \sum_{k=1}^K \|\Delta\boldsymbol{\mu}(\mathbf{y}_k)\|_2^2 = \frac{1}{K} \sum_{k=1}^K \|\mathbf{M}\mathbf{y}_k^{\mathcal{F}} + \mathbf{b}\|_2^2 \\
 &= \frac{1}{K} \sum_{k=1}^K (\mathbf{y}_k^{\mathcal{F}})^T \mathbf{M}^T \mathbf{M} \mathbf{y}_k^{\mathcal{F}} + 2\mathbf{b}^T \mathbf{M} \mathbf{y}_k^{\mathcal{F}} + \mathbf{b}^T \mathbf{b} \\
 &= \text{Tr} \left( \mathbf{M}^T \mathbf{M} \frac{1}{K} \sum_{k=1}^K \mathbf{y}_k^{\mathcal{F}} (\mathbf{y}_k^{\mathcal{F}})^T \right) + 2\mathbf{b}^T \mathbf{M} \boldsymbol{\mu}_y^{\mathcal{F}} + \mathbf{b}^T \mathbf{b} \\
 &= \text{Tr} \left( \mathbf{M}^T \mathbf{M} (\boldsymbol{\Lambda}_y + \boldsymbol{\mu}_y^{\mathcal{F}} (\boldsymbol{\mu}_y^{\mathcal{F}})^T) \right) + 2\mathbf{b}^T \mathbf{M} \boldsymbol{\mu}_y^{\mathcal{F}} + \mathbf{b}^T \mathbf{b} \\
 &= \text{Tr}(\mathbf{M}^T \mathbf{M} \boldsymbol{\Lambda}_y) + \|\mathbf{M} \boldsymbol{\mu}_y^{\mathcal{F}} + \mathbf{b}\|_2^2
 \end{aligned} \tag{49}$$

where

$$\boldsymbol{\mu}_y^{\mathcal{F}} = \frac{1}{K} \sum_{k=1}^K \mathbf{y}_k^{\mathcal{F}}, \quad \boldsymbol{\Lambda}_y = \frac{1}{K} \sum_{k=1}^K (\mathbf{y}_k^{\mathcal{F}} - \boldsymbol{\mu}_y^{\mathcal{F}}) (\mathbf{y}_k^{\mathcal{F}} - \boldsymbol{\mu}_y^{\mathcal{F}})^T$$

denote the empirical mean and covariance of  $\mathbf{y}$  in the frequency domain.

Substituting 49 into the average Wasserstein distance 48 yields:

$$\begin{aligned}
 [\mathcal{L}_{W_2}^2]_{\text{Avg}} &= \frac{1}{K} \sum_{k=1}^K \left( \sum_i \left( \sqrt{\lambda_0^{(i)}} - \mathbf{D}_1^{(i)} \right)^2 + \sum_i \left( \boldsymbol{\mu}_{\mathbf{x}^{\mathcal{F}}|\mathbf{y},k}^{(i)} - \boldsymbol{\mu}_{\hat{\mathbf{x}}^{\mathcal{F}}|\mathbf{y},k}^{(i)} \right)^2 \right) \\
 &= \sum_i \left( \sqrt{\lambda_0^{(i)}} - \mathbf{D}_1^{(i)} \right)^2 + \text{Tr}(\mathbf{M}^T \mathbf{M} \boldsymbol{\Lambda}_y) + \|\mathbf{M} \boldsymbol{\mu}_y^{\mathcal{F}} + \mathbf{b}\|_2^2
 \end{aligned} \tag{50}$$

Using the true distribution of  $\mathbf{y}$  in terms of the prior, as in 41, we have:

$$\boldsymbol{\mu}_y^{\mathcal{F}} = \boldsymbol{\Lambda}_h \boldsymbol{\mu}_x^{\mathcal{F}}, \quad \boldsymbol{\Lambda}_y = \boldsymbol{\Lambda}_h \boldsymbol{\Lambda}_0 \boldsymbol{\Lambda}_{h^*} + \sigma_n^2 \mathbf{I}$$

Substituting these expressions into 50, the average Wasserstein-2 distance can be written as:

$$[\mathcal{L}_{W_2}^2]_{\text{Avg}} = \sum_i \left( \sqrt{\lambda_0^{(i)}} - \mathbf{D}_1^{(i)} \right)^2 + \text{Tr} \left( \mathbf{M}^T \mathbf{M} (\boldsymbol{\Lambda}_h \boldsymbol{\Lambda}_0 \boldsymbol{\Lambda}_{h^*} + \sigma_n^2 \mathbf{I}) \right) + \|\mathbf{M} \boldsymbol{\Lambda}_h \boldsymbol{\mu}_x^{\mathcal{F}} + \mathbf{b}\|_2^2 \tag{51}$$

## F. DPS algorithm

In this section, we present the DPS algorithm (Chung et al., 2022a) from a spectral perspective and show how it can be integrated into our method.

As discussed in Section 2.3, to avoid retraining a model for a specific degradation matrix  $\mathbf{H}$ , DPS (Chung et al., 2022a) uses a Bayesian formulation, in which the posterior score gradient is expressed as

$$\nabla_{\mathbf{x}_t} \log p_t(\mathbf{x}_t|\mathbf{y}) = \nabla_{\mathbf{x}_t} \log p_t(\mathbf{x}_t) + \nabla_{\mathbf{x}_t} \log p_t(\mathbf{y}|\mathbf{x}_t) \tag{52}$$

While the first term can be obtained directly from a pretrained prior model, the second term is expressed by marginalizing over  $\mathbf{x}_0$ :

$$p(\mathbf{y}|\mathbf{x}_t) = \int_{\mathbf{x}_0} p(\mathbf{x}_0|\mathbf{x}_t) p(\mathbf{y}|\mathbf{x}_0) d\mathbf{x}_0 \tag{53}$$

Here, the conditional probability  $p(\mathbf{y}|\mathbf{x}_0)$  is determined by the linear observation model  $\mathbf{y} = \mathbf{H}\mathbf{x}_0 + \mathbf{n}$ , which implies a Gaussian distribution:

$$p(\mathbf{y}|\mathbf{x}_0) = \mathcal{N}(\mathbf{H}\mathbf{x}_0, \sigma_y^2 \mathbf{I})$$

$$p(\mathbf{y}|\mathbf{x}_0) = \frac{1}{\sqrt{(2\pi)^d \sigma_y^2}} \exp \left[ -\frac{\|\mathbf{y} - \mathbf{H}\mathbf{x}_0\|_2^2}{2\sigma^2} \right]$$

A key approximation in DPS is modeling the distribution  $p(\mathbf{x}_0|\mathbf{x}_t)$  as a deterministic Gaussian centered at the estimated mean:

$$p(\mathbf{x}_0|\mathbf{x}_t) \approx \mathcal{N}(\hat{\mathbf{x}}_0, \mathbf{0})$$

Applying this deterministic model in (53) gives a closed-form expression for the conditional likelihood:

$$p_t(\mathbf{y}|\mathbf{x}_t) \approx \mathcal{N}(\mathbf{H}\hat{\mathbf{x}}_0, \sigma_y^2 \mathbf{I})$$

which leads to the gradient:

$$\nabla_{\mathbf{x}_t} \log p_t(\mathbf{y}|\mathbf{x}_t) \simeq -\frac{1}{\sigma_y^2} \nabla_{\mathbf{x}_t} \|\mathbf{y} - \mathbf{H}\hat{\mathbf{x}}_0\|_2^2$$

The authors of (Chung et al., 2022a) reweight this term using the heuristic  $\zeta_i = \zeta'/|\mathbf{y} - \mathbf{H}\hat{\mathbf{x}}_0(\mathbf{x}_s)|$ , which scales the step size inversely with the norm of the measurement error, where  $\zeta'$  is a user-defined constant.

$$\nabla_{\mathbf{x}_t} \log p_t(\mathbf{y}|\mathbf{x}_t) \simeq -\zeta_i \nabla_{\mathbf{x}_t} \|\mathbf{y} - \mathbf{H}\hat{\mathbf{x}}_0\|_2^2$$

### F.1. The Reverse Process in the Time Domain (DPS)

The original formulation of the DPS algorithm is based on DDPM (Ho et al., 2020). Here, we present it (Chung et al., 2022a) within the DDIM (Song et al., 2021) framework under the Variance-Preserving (VP) parameterization (Song et al., 2020).

$$\mathbf{x}_{s-1} = \sqrt{\bar{\alpha}_{t-1}} \hat{\mathbf{x}}_0 + \sqrt{1 - \bar{\alpha}_{t-1} - \sigma_s^2(\eta)} \epsilon_\theta(\mathbf{x}_s, s) - \zeta_i \nabla_{\mathbf{x}_t} \|\mathbf{y} - \mathbf{H}\hat{\mathbf{x}}_0\|_2^2 + \sigma_s(\eta) \mathbf{z}_s. \quad (54)$$

where:

$$\sigma_s(\eta) = \eta \sqrt{\frac{1 - \bar{\alpha}_{s-1}}{1 - \bar{\alpha}_s}} \sqrt{1 - \frac{\bar{\alpha}_s}{\bar{\alpha}_{s-1}}}.$$

We consider the deterministic setting, corresponding to  $\eta = 0$ .

$$\mathbf{x}_{s-1} = \sqrt{\bar{\alpha}_{s-1}} \hat{\mathbf{x}}_0 + \sqrt{1 - \bar{\alpha}_{s-1}} \epsilon_\theta(\mathbf{x}_s, s) - \zeta_i \nabla_{\mathbf{x}_t} \|\mathbf{y} - \mathbf{H}\hat{\mathbf{x}}_0\|_2^2$$

Using the marginal property,

$$\epsilon_\theta(\mathbf{x}_s, s) = \frac{\mathbf{x}_s - \sqrt{\bar{\alpha}_s} \hat{\mathbf{x}}_0}{\sqrt{1 - \bar{\alpha}_s}}. \quad (55)$$

which, substituted into Equation 54, gives:

$$\mathbf{x}_{s-1} = \sqrt{\bar{\alpha}_{s-1}} \hat{\mathbf{x}}_0 + \sqrt{1 - \bar{\alpha}_{s-1}} \left[ \frac{\mathbf{x}_s - \sqrt{\bar{\alpha}_s} \hat{\mathbf{x}}_0}{\sqrt{1 - \bar{\alpha}_s}} \right] - \zeta_i \nabla_{\mathbf{x}_t} \|\mathbf{y} - \mathbf{H}\hat{\mathbf{x}}_0\|_2^2$$

$$\mathbf{x}_{s-1} = \frac{\sqrt{1 - \bar{\alpha}_{s-1}}}{\sqrt{1 - \bar{\alpha}_s}} \mathbf{x}_s + \left[ \sqrt{\bar{\alpha}_{s-1}} - \frac{\sqrt{\bar{\alpha}_s} \sqrt{1 - \bar{\alpha}_{s-1}}}{\sqrt{1 - \bar{\alpha}_s}} \right] \hat{\mathbf{x}}_0 - \zeta_i \nabla_{\mathbf{x}_t} \|\mathbf{y} - \mathbf{H}\hat{\mathbf{x}}_0\|_2^2$$

Introducing:

$$a_s = \left[ \frac{\sqrt{1 - \bar{\alpha}_{s-1}}}{\sqrt{1 - \bar{\alpha}_s}} \right] \mathbf{I}$$

$$b_s = \left[ \sqrt{\bar{\alpha}_{s-1}} - \frac{\sqrt{\bar{\alpha}_s} \sqrt{1 - \bar{\alpha}_{s-1}}}{\sqrt{1 - \bar{\alpha}_s}} \right] \mathbf{I}$$

we obtain:

$$\mathbf{x}_{s-1} = a_s \mathbf{x}_s + b_s \hat{\mathbf{x}}_0 - \zeta_i \nabla_{\mathbf{x}_t} \|\mathbf{y} - \mathbf{H}\hat{\mathbf{x}}_0\|_2^2$$

Where  $\hat{\mathbf{x}}_0$  denotes the MMSE denoiser, corresponds to the denoised signal produced by a pretrained network. Assuming a Gaussian prior, the optimal solution  $\mathbf{x}_0^*$  is given by (Benita et al., 2025):

$$\mathbf{x}_0^* = (\bar{\alpha}_s \boldsymbol{\Sigma}_0 + (1 - \bar{\alpha}_s) \mathbf{I})^{-1} (\sqrt{\bar{\alpha}_s} \boldsymbol{\Sigma}_0 \mathbf{x}_s + (1 - \bar{\alpha}_s) \boldsymbol{\mu}_0)$$

Therefore we get:

$$\boxed{\mathbf{x}_{s-1} = a_s \mathbf{x}_s + b_s \mathbf{x}_0^* - \zeta_i \nabla_{\mathbf{x}_t} \|\mathbf{y} - \mathbf{H} \mathbf{x}_0^*\|_2^2} \quad (56)$$

Since  $\mathbf{x}_0^*$  depends on  $\mathbf{x}_s$  we denote it as  $\mathbf{x}_0^*(\mathbf{x}_s)$ :

$$\zeta_i \nabla_{\mathbf{x}_s} \|\mathbf{y} - \mathbf{H} \mathbf{x}_0^*\|_2^2 = \zeta_i \nabla_{\mathbf{x}_s} \|\mathbf{y} - \mathbf{H} \mathbf{x}_0^*(\mathbf{x}_s)\|_2^2$$

Hence, the gradient can be written as:

$$\zeta_i \nabla_{\mathbf{x}_t} \|\mathbf{y} - \mathbf{H} \mathbf{x}_0^*\|_2^2 = \zeta_i \left[ -2 [\nabla_{\mathbf{x}_s} \mathbf{x}_0^*(\mathbf{x}_s)]^T \mathbf{H}^T (\mathbf{y} - \mathbf{H} \mathbf{x}_0^*(\mathbf{x}_s)) \right]$$

Where:

$$\nabla_{\mathbf{x}_s} \mathbf{x}_0^*(\mathbf{x}_s) = \nabla_{\mathbf{x}_s} \left[ (\bar{\alpha}_s \boldsymbol{\Sigma}_0 + (1 - \bar{\alpha}_s) \mathbf{I})^{-1} (\sqrt{\bar{\alpha}_s} \boldsymbol{\Sigma}_0 \mathbf{x}_s + (1 - \bar{\alpha}_s) \boldsymbol{\mu}_0) \right]$$

$$\nabla_{\mathbf{x}_s} \mathbf{x}_0^*(\mathbf{x}_s) = (\bar{\alpha}_s \boldsymbol{\Sigma}_0 + (1 - \bar{\alpha}_s) \mathbf{I})^{-1} \sqrt{\bar{\alpha}_s} \boldsymbol{\Sigma}_0 \quad (57)$$

This yields:

$$\zeta_i \nabla_{\mathbf{x}_s} \|\mathbf{y} - \mathbf{H} \mathbf{x}_0^*\|_2^2 = \zeta_i \left[ -2 \sqrt{\bar{\alpha}_s} \boldsymbol{\Sigma}_0 (\bar{\alpha}_s \boldsymbol{\Sigma}_0 + (1 - \bar{\alpha}_s) \mathbf{I})^{-1} \mathbf{H}^T (\mathbf{y} - \mathbf{H} \mathbf{x}_0^*(\mathbf{x}_s)) \right]$$

Substituting into (56) gives:

$$\boxed{\mathbf{x}_{s-1} = a_s \mathbf{x}_s + b_s \mathbf{x}_0^* + 2\zeta_i \left[ \sqrt{\bar{\alpha}_s} \boldsymbol{\Sigma}_0 (\bar{\alpha}_s \boldsymbol{\Sigma}_0 + (1 - \bar{\alpha}_s) \mathbf{I})^{-1} \mathbf{H}^T (\mathbf{y} - \mathbf{H} \mathbf{x}_0^*) \right]} \quad (58)$$

## F.2. Migrating to the spectral Domain

Next, we apply the Discrete Fourier Transform (DFT), denoted by  $\mathcal{F}$ , to Equation (58). Assuming that  $\boldsymbol{\Sigma}_0$  and  $\mathbf{H}$  are shift-invariant, both matrices are diagonalized by the DFT. Specifically we denote:

$$\begin{aligned} \mathbf{F} \mathbf{H} \mathbf{F}^T &= \boldsymbol{\Lambda}_h = \text{diag}(h_1, h_2, \dots, h_d), \\ \mathbf{F} \mathbf{H}^T \mathbf{F}^T &= \boldsymbol{\Lambda}_h^* = \text{diag}(\bar{h}_1, \bar{h}_2, \dots, \bar{h}_d), \\ \mathbf{F} \mathbf{H}^T \mathbf{H} \mathbf{F}^T &= \boldsymbol{\Lambda}_{|h|^2} = \text{diag}(|h_1|^2, |h_2|^2, \dots, |h_d|^2). \end{aligned}$$

Applying the unitary Fourier operator  $\mathbf{F}$  transforms Equation (58) into the frequency domain.

$$\begin{aligned} \mathbf{F} \mathbf{x}_{s-1} &= \mathbf{F} \left[ a_s \mathbf{x}_s + b_s \mathbf{x}_0^* + 2\zeta_i \left[ \sqrt{\bar{\alpha}_s} \boldsymbol{\Sigma}_0 (\bar{\alpha}_s \boldsymbol{\Sigma}_0 + (1 - \bar{\alpha}_s) \mathbf{I})^{-1} \mathbf{H}^T (\mathbf{y} - \mathbf{H} \mathbf{x}_0^*) \right] \right] \\ \mathbf{x}_{s-1}^{\mathcal{F}} &= a_s \mathbf{x}_s^{\mathcal{F}} + b_s \mathbf{F} \mathbf{x}_0^* + 2\zeta_i \mathbf{F} \left[ \sqrt{\bar{\alpha}_s} \boldsymbol{\Sigma}_0 (\bar{\alpha}_s \boldsymbol{\Sigma}_0 + (1 - \bar{\alpha}_s) \mathbf{I})^{-1} \mathbf{H}^T (\mathbf{y} - \mathbf{H} \mathbf{x}_0^*) \right] \end{aligned} \quad (59)$$

Where:

$$\begin{aligned} \mathbf{F} \mathbf{x}_0^* &= \mathbf{F} \left[ (\bar{\alpha}_s \boldsymbol{\Sigma}_0 + (1 - \bar{\alpha}_s) \mathbf{I})^{-1} (\sqrt{\bar{\alpha}_s} \boldsymbol{\Sigma}_0 \mathbf{x}_s + (1 - \bar{\alpha}_s) \boldsymbol{\mu}_0) \right] \\ &= \mathbf{F} (\bar{\alpha}_s \boldsymbol{\Sigma}_0 + (1 - \bar{\alpha}_s) \mathbf{I})^{-1} \mathbf{F}^T \mathbf{F} (\sqrt{\bar{\alpha}_s} \boldsymbol{\Sigma}_0 \mathbf{x}_s + (1 - \bar{\alpha}_s) \boldsymbol{\mu}_0) \\ &= [\bar{\alpha}_s \boldsymbol{\Lambda}_0 + (1 - \bar{\alpha}_s) \mathbf{I}]^{-1} (\sqrt{\bar{\alpha}_s} \mathbf{F} \boldsymbol{\Sigma}_0 \mathbf{F}^T \mathbf{x}_s + (1 - \bar{\alpha}_s) \mathbf{F} \boldsymbol{\mu}_0) \end{aligned}$$

$$\mathbf{F} \mathbf{x}_0^* = [\bar{\alpha}_s \boldsymbol{\Lambda}_0 + (1 - \bar{\alpha}_s) \mathbf{I}]^{-1} (\sqrt{\bar{\alpha}_s} \boldsymbol{\Lambda}_0 \mathbf{x}_s^{\mathcal{F}} + (1 - \bar{\alpha}_s) \boldsymbol{\mu}_0^{\mathcal{F}}) \quad (60)$$

and:

$$\begin{aligned}
 & \mathbf{F} \left[ \sqrt{\bar{\alpha}_s} \boldsymbol{\Sigma}_0 (\bar{\alpha}_s \boldsymbol{\Sigma}_0 + (1 - \bar{\alpha}_s) \mathbf{I})^{-1} \mathbf{H}^T (\mathbf{y} - \mathbf{H} \mathbf{x}_0^*) \right] \\
 &= \left[ \sqrt{\bar{\alpha}_s} \mathbf{F} \boldsymbol{\Sigma}_0 \mathbf{F}^T \mathbf{F} (\bar{\alpha}_s \boldsymbol{\Sigma}_0 + (1 - \bar{\alpha}_s) \mathbf{I})^{-1} \mathbf{F}^T \mathbf{F} \mathbf{H}^T \mathbf{F}^T \mathbf{F} (\mathbf{y} - \mathbf{H} \mathbf{x}_0^*) \right] \\
 &= \left[ \sqrt{\bar{\alpha}_s} \boldsymbol{\Lambda}_0 [\bar{\alpha}_s \boldsymbol{\Lambda}_0 + (1 - \bar{\alpha}_s) \mathbf{I}]^{-1} \boldsymbol{\Lambda}_{h^*} (\mathbf{F} \mathbf{y} - \mathbf{F} \mathbf{H} \mathbf{F}^T \mathbf{F} \mathbf{x}_0^*) \right] \\
 &= \left[ \sqrt{\bar{\alpha}_s} \boldsymbol{\Lambda}_0 [\bar{\alpha}_s \boldsymbol{\Lambda}_0 + (1 - \bar{\alpha}_s) \mathbf{I}]^{-1} \boldsymbol{\Lambda}_{h^*} (\mathbf{F} \mathbf{y} - \mathbf{F} \mathbf{H} \mathbf{F}^T \mathbf{F} \mathbf{x}_0^*) \right] \\
 &= \left[ \sqrt{\bar{\alpha}_s} \boldsymbol{\Lambda}_0 [\bar{\alpha}_s \boldsymbol{\Lambda}_0 + (1 - \bar{\alpha}_s) \mathbf{I}]^{-1} \boldsymbol{\Lambda}_{h^*} (\mathbf{y}^{\mathcal{F}} - \boldsymbol{\Lambda}_h \mathbf{F} \mathbf{x}_0^*) \right]. \tag{61}
 \end{aligned}$$

By defining:

$$\begin{aligned}
 c_s &= \sqrt{\bar{\alpha}_s} \boldsymbol{\Lambda}_0 [\bar{\alpha}_s \boldsymbol{\Lambda}_0 + (1 - \bar{\alpha}_s) \mathbf{I}]^{-1} \\
 d_s &= (1 - \bar{\alpha}_s) [\bar{\alpha}_s \boldsymbol{\Lambda}_0 + (1 - \bar{\alpha}_s) \mathbf{I}]^{-1}
 \end{aligned}$$

Equation 60 can be rewritten as:

$$\mathbf{F} \mathbf{x}_0^* = c_s \mathbf{x}_s^{\mathcal{F}} + d_s \boldsymbol{\mu}_0^{\mathcal{F}} \tag{62}$$

Substitute it into Equation 61, we get:

$$\mathbf{F} \left[ \sqrt{\bar{\alpha}_s} \boldsymbol{\Sigma}_0 (\bar{\alpha}_s \boldsymbol{\Sigma}_0 + (1 - \bar{\alpha}_s) \mathbf{I})^{-1} \mathbf{H}^T (\mathbf{y} - \mathbf{H} \mathbf{x}_0^*) \right] = [c_s \boldsymbol{\Lambda}_{h^*} (\mathbf{y}^{\mathcal{F}} - \boldsymbol{\Lambda}_h (c_s \mathbf{x}_s^{\mathcal{F}} + d_s \boldsymbol{\mu}_0^{\mathcal{F}}))]$$

Finally, Equation 59 can be rewritten as:

$$\begin{aligned}
 \mathbf{x}_{t-1}^{\mathcal{F}} &= a_s \mathbf{x}_s^{\mathcal{F}} + b_s [c_s \mathbf{x}_s^{\mathcal{F}} + d_s \boldsymbol{\mu}_0^{\mathcal{F}}] + 2\zeta_i [c_s \boldsymbol{\Lambda}_{h^*} (\mathbf{y}^{\mathcal{F}} - \boldsymbol{\Lambda}_h (c_s \mathbf{x}_s^{\mathcal{F}} + d_s \boldsymbol{\mu}_0^{\mathcal{F}}))] \\
 \mathbf{x}_{t-1}^{\mathcal{F}} &= [a_s + b_s c_s - 2\zeta_i c_s \boldsymbol{\Lambda}_{h^*} \boldsymbol{\Lambda}_h c_s] \mathbf{x}_s^{\mathcal{F}} + [2\zeta_i c_s \boldsymbol{\Lambda}_{h^*}] \mathbf{y}^{\mathcal{F}} + [b_s d_s - 2\zeta_i c_s \boldsymbol{\Lambda}_{h^*} \boldsymbol{\Lambda}_h d_s] \boldsymbol{\mu}_0^{\mathcal{F}}
 \end{aligned}$$

Denoting:

$$\begin{aligned}
 \mathbf{G}(s) &= [a_s + b_s c_s - 2\zeta_i c_s \boldsymbol{\Lambda}_{h^*} \boldsymbol{\Lambda}_h c_s] \\
 \mathbf{Q}(s) &= [2\zeta_i c_s \boldsymbol{\Lambda}_{h^*}] \\
 \mathbf{M}(s) &= [b_s d_s - 2\zeta_i c_s \boldsymbol{\Lambda}_{h^*} \boldsymbol{\Lambda}_h d_s]
 \end{aligned}$$

$$\mathbf{x}_{s-1}^{\mathcal{F}} = \mathbf{G}(s) \mathbf{x}_s^{\mathcal{F}} + \mathbf{Q}(s) \mathbf{y}^{\mathcal{F}} + \mathbf{M}(s) \boldsymbol{\mu}_0^{\mathcal{F}} \tag{63}$$

By recursively applying Equation (63), we obtain a frequency-domain representation for each diffusion step  $\mathbf{x}_l^{\mathcal{F}}$ :

$$\mathbf{x}_l^{\mathcal{F}} = \left[ \prod_{j=l+1}^S \mathbf{G}(j) \right] \mathbf{x}_S^{\mathcal{F}} + \left[ \sum_{i=l+1}^S \left( \prod_{j=l+1}^{i-1} \mathbf{G}(j) \right) \mathbf{Q}(i) \right] \mathbf{y}^{\mathcal{F}} + \left[ \sum_{i=l+1}^S \left( \prod_{j=l+1}^{i-1} \mathbf{G}(j) \right) \mathbf{M}(i) \right] \boldsymbol{\mu}_0^{\mathcal{F}}$$

Specifically for  $l = 0$ :

$$\mathbf{x}_0^{\mathcal{F}} = \left[ \prod_{j=1}^S \mathbf{G}(j) \right] \mathbf{x}_S^{\mathcal{F}} + \left[ \sum_{i=1}^S \left( \prod_{j=1}^{i-1} \mathbf{G}(j) \right) \mathbf{Q}(i) \right] \mathbf{y}^{\mathcal{F}} + \left[ \sum_{i=1}^S \left( \prod_{j=1}^{i-1} \mathbf{G}(j) \right) \mathbf{M}(i) \right] \boldsymbol{\mu}_0^{\mathcal{F}}$$

Denoting:

$$\begin{aligned}
 \mathbf{D}_1 &= \prod_{j=l+1}^S \mathbf{G}(j) \\
 \mathbf{D}_2 &= \sum_{i=l+1}^S \left( \prod_{j=l+1}^{i-1} \mathbf{G}(j) \right) \mathbf{Q}(i)
 \end{aligned}$$

$$\mathbf{D}_3 = \sum_{i=l+1}^S \left( \prod_{j=l+1}^{i-1} \mathbf{G}(j) \right) \mathbf{M}(i)$$

$$\mathbf{x}_0^{\mathcal{F}} = \mathbf{D}_1 \mathbf{x}_S^{\mathcal{F}} + \mathbf{D}_2 \mathbf{y}^{\mathcal{F}} + \mathbf{D}_3 \boldsymbol{\mu}_0^{\mathcal{F}} \quad (64)$$

Equation 64 can be interpreted as a transfer function, describing the relationship between the input Gaussian noise  $\mathbf{x}_S^{\mathcal{F}} \sim \mathcal{N}(\mathbf{0}, \mathbf{I})$  and the estimated output signal  $\mathbf{x}_{0,\text{DPS}}^{\mathcal{F}}$ . The output signal is also Gaussian, with the following distributional properties:

**Mean:**

$$\mathbb{E} [\mathbf{x}_0^{\mathcal{F}}] = \mathbf{D}_2 \mathbf{y}^{\mathcal{F}} + \mathbf{D}_3 \boldsymbol{\mu}_0^{\mathcal{F}}$$

**Covariance:**

$$\boldsymbol{\Sigma}_{\mathbf{x}_0^{\mathcal{F}}} = \mathbb{E} \left[ [\mathbf{x}_0^{\mathcal{F}} - \mathbb{E} [\mathbf{x}_0^{\mathcal{F}}]] [\mathbf{x}_0^{\mathcal{F}} - \mathbb{E} [\mathbf{x}_0^{\mathcal{F}}]]^T \right] = [\mathbf{D}_1]^2$$

$$\hat{\mathbf{x}}_0^{\mathcal{F}} \sim \mathcal{N}(\mathbf{D}_2 \mathbf{y}^{\mathcal{F}} + \mathbf{D}_3 \boldsymbol{\mu}_0^{\mathcal{F}}, \mathbf{D}_1^2) \quad (65)$$

## G. II GDM algorithm

The II GDM method shares the same Bayesian principle as DPS, but differs in its approximation of the likelihood term. Specifically,  $p(\mathbf{y}|\mathbf{x}_t)$  is modeled as a Gaussian distribution with covariance that varies across diffusion time steps  $t$ :

$$p_t(\mathbf{y}|\mathbf{x}_t) \approx \mathcal{N}(\mathbf{H}\hat{\mathbf{x}}_0, r_t^2 \mathbf{H}\mathbf{H}^T + \sigma_y^2 \mathbf{I})$$

Thus, the gradient of the log-probability is given by:

$$\nabla_{\mathbf{x}_t} \log p_t(\mathbf{y}|\mathbf{x}_t) \approx \nabla_{\mathbf{x}_t} (\hat{\mathbf{x}}_0)^T \mathbf{H}^T ((r_t^2 \mathbf{H}\mathbf{H}^T + \sigma_y^2 \mathbf{I})^{-1})^T (\mathbf{y} - \mathbf{H}\hat{\mathbf{x}}_0)$$

### G.1. The Reverse Process in the Time Domain (Paper Version)

Based on the DDIM (Song et al., 2021) inference process and the Variance-Preserving (VP) framework, the inference procedure using II GDM is formulated as:

$$\begin{aligned} \mathbf{x}_{s-1} = & \sqrt{\bar{\alpha}_{s-1}} \hat{\mathbf{x}}_0 + \sqrt{1 - \bar{\alpha}_{s-1} - \sigma_s^2(\eta)} \boldsymbol{\epsilon}_\theta(\mathbf{x}_s, s) \\ & + \sqrt{\bar{\alpha}_s} \nabla_{\mathbf{x}_s} (\hat{\mathbf{x}}_0)^T \mathbf{H}^T ((r_s^2 \mathbf{H}\mathbf{H}^T + \sigma_y^2 \mathbf{I})^{-1})^T (\mathbf{y} - \mathbf{H}\hat{\mathbf{x}}_0) + \sigma_s(\eta) \mathbf{z}_s. \end{aligned} \quad (66)$$

where:

$$\sigma_s(\eta) = \eta \sqrt{\frac{1 - \bar{\alpha}_{s-1}}{1 - \bar{\alpha}_s}} \sqrt{1 - \frac{\bar{\alpha}_s}{\bar{\alpha}_{s-1}}}.$$

Since the VP formulation is already used for  $\hat{\mathbf{x}}_0$ , we omit the conversion factor  $\sqrt{\bar{\alpha}_t}$  in the gradient term, leading to:

$$\begin{aligned} \mathbf{x}_{s-1} = & \sqrt{\bar{\alpha}_{s-1}} \hat{\mathbf{x}}_0 + \sqrt{1 - \bar{\alpha}_{s-1} - \sigma_s^2(\eta)} \boldsymbol{\epsilon}_\theta(\mathbf{x}_s, s) \\ & + \nabla_{\mathbf{x}_s} (\hat{\mathbf{x}}_0)^T \mathbf{H}^T ((r_s^2 \mathbf{H}\mathbf{H}^T + \sigma_y^2 \mathbf{I})^{-1})^T (\mathbf{y} - \mathbf{H}\hat{\mathbf{x}}_0) + \sigma_s(\eta) \mathbf{z}_s. \end{aligned} \quad (67)$$

By using the deterministic process ( $\eta = 0$ ):

$$\begin{aligned} \mathbf{x}_{s-1} = & \sqrt{\bar{\alpha}_{s-1}} \hat{\mathbf{x}}_0 + \sqrt{1 - \bar{\alpha}_{s-1}} \boldsymbol{\epsilon}_\theta(\mathbf{x}_s, s) \\ & + \nabla_{\mathbf{x}_s} (\hat{\mathbf{x}}_0)^T \mathbf{H}^T ((r_s^2 \mathbf{H}\mathbf{H}^T + \sigma_y^2 \mathbf{I})^{-1})^T (\mathbf{y} - \mathbf{H}\hat{\mathbf{x}}_0) \end{aligned} \quad (68)$$

Using the marginal property,

$$\boldsymbol{\epsilon}_\theta(\mathbf{x}_s, s) = \frac{\mathbf{x}_s - \sqrt{\bar{\alpha}_s} \hat{\mathbf{x}}_0}{\sqrt{1 - \bar{\alpha}_s}}. \quad (69)$$

which, substituted into Equation 68, gives:

$$\begin{aligned}\mathbf{x}_{s-1} &= \sqrt{\bar{\alpha}_{s-1}} \hat{\mathbf{x}}_0 + \sqrt{1 - \bar{\alpha}_{s-1}} \left[ \frac{\mathbf{x}_s - \sqrt{\bar{\alpha}_s} \hat{\mathbf{x}}_0}{\sqrt{1 - \bar{\alpha}_s}} \right] + \nabla_{\mathbf{x}_s}(\hat{\mathbf{x}}_0)^T \mathbf{H}^T ((r_s^2 \mathbf{H} \mathbf{H}^T + \sigma_y^2 \mathbf{I})^{-1})^T (\mathbf{y} - \mathbf{H} \hat{\mathbf{x}}_0) \\ &= \frac{\sqrt{1 - \bar{\alpha}_{s-1}}}{\sqrt{1 - \bar{\alpha}_s}} \mathbf{x}_s + \left[ \sqrt{\bar{\alpha}_{s-1}} - \frac{\sqrt{\bar{\alpha}_s} \sqrt{1 - \bar{\alpha}_{s-1}}}{\sqrt{1 - \bar{\alpha}_s}} \right] \hat{\mathbf{x}}_0 + \nabla_{\mathbf{x}_s}(\hat{\mathbf{x}}_0)^T \mathbf{H}^T ((r_s^2 \mathbf{H} \mathbf{H}^T + \sigma_y^2 \mathbf{I})^{-1})^T (\mathbf{y} - \mathbf{H} \hat{\mathbf{x}}_0)\end{aligned}$$

Introducing:

$$\begin{aligned}a_s &= \left[ \frac{\sqrt{1 - \bar{\alpha}_{s-1}}}{\sqrt{1 - \bar{\alpha}_s}} \right] \mathbf{I} \\ b_s &= \left[ \sqrt{\bar{\alpha}_{s-1}} - \frac{\sqrt{\bar{\alpha}_s} \sqrt{1 - \bar{\alpha}_{s-1}}}{\sqrt{1 - \bar{\alpha}_s}} \right] \mathbf{I}\end{aligned}$$

we obtain:

$$\boxed{\mathbf{x}_{s-1} = a_s \mathbf{x}_s + b_s \hat{\mathbf{x}}_0 + \nabla_{\mathbf{x}_s}(\hat{\mathbf{x}}_0)^T \mathbf{H}^T ((r_s^2 \mathbf{H} \mathbf{H}^T + \sigma_y^2 \mathbf{I})^{-1})^T (\mathbf{y} - \mathbf{H} \hat{\mathbf{x}}_0)} \quad (70)$$

Where  $\hat{\mathbf{x}}_0$  denotes the MMSE denoiser, corresponds to the denoised signal produced by a pretrained network. Assuming a Gaussian prior, the optimal solution  $\mathbf{x}_0^*$  is given by (Benita et al., 2025):

$$\mathbf{x}_0^* = (\bar{\alpha}_s \boldsymbol{\Sigma}_0 + (1 - \bar{\alpha}_s) \mathbf{I})^{-1} (\sqrt{\bar{\alpha}_s} \boldsymbol{\Sigma}_0 \mathbf{x}_s + (1 - \bar{\alpha}_s) \boldsymbol{\mu}_0)$$

Therefore we get:

$$\mathbf{x}_{s-1} = a_s \mathbf{x}_s + b_s \mathbf{x}_0^* + \nabla_{\mathbf{x}_s}(\mathbf{x}_0^*(\mathbf{x}_s))^T \mathbf{H}^T ((r_s^2 \mathbf{H} \mathbf{H}^T + \sigma_y^2 \mathbf{I})^{-1})^T (\mathbf{y} - \mathbf{H} \mathbf{x}_0^*)$$

from Equation 57:

$$\nabla_{\mathbf{x}_s} \mathbf{x}_0^*(\mathbf{x}_s) = (\bar{\alpha}_s \boldsymbol{\Sigma}_0 + (1 - \bar{\alpha}_s) \mathbf{I})^{-1} \sqrt{\bar{\alpha}_s} \boldsymbol{\Sigma}_0$$

Using the property  $(\mathbf{A}^{-1})^T = (\mathbf{A}^T)^{-1}$  for any invertible matrix  $\mathbf{A}$ , with  $\mathbf{A} = \alpha_s \boldsymbol{\Sigma}_0 + (1 - \alpha_s) \mathbf{I}$ , it can be rewritten as:

$$\nabla_{\mathbf{x}_s} \mathbf{x}_0^*(\mathbf{x}_s)^T = \sqrt{\bar{\alpha}_s} \boldsymbol{\Sigma}_0 (\bar{\alpha}_s \boldsymbol{\Sigma}_0 + (1 - \bar{\alpha}_s) \mathbf{I})^{-1}$$

Substitute it into Equation 70, we get:

$$\boxed{\mathbf{x}_{s-1} = a_s \mathbf{x}_s + b_s \mathbf{x}_0^* + \sqrt{\bar{\alpha}_s} \boldsymbol{\Sigma}_0 (\bar{\alpha}_s \boldsymbol{\Sigma}_0 + (1 - \bar{\alpha}_s) \mathbf{I})^{-1} \mathbf{H}^T (r_s^2 \mathbf{H} \mathbf{H}^T + \sigma_y^2 \mathbf{I})^{-1} (\mathbf{y} - \mathbf{H} \mathbf{x}_0^*)} \quad (71)$$

## G.2. Migrating to the spectral Domain

Next, we apply the Discrete Fourier Transform (DFT), denoted by  $\mathcal{F} \cdot$ , to Equation (71). Assuming that  $\boldsymbol{\Sigma}_0$  and  $\mathbf{H}$  are shift-invariant, both matrices are diagonalized by the DFT.

$$\mathbf{F} \mathbf{x}_{s-1} = \mathbf{F} [a_s \mathbf{x}_s + b_s \mathbf{x}_0^* + \sqrt{\bar{\alpha}_s} \boldsymbol{\Sigma}_0 (\bar{\alpha}_s \boldsymbol{\Sigma}_0 + (1 - \bar{\alpha}_s) \mathbf{I})^{-1} \mathbf{H}^T (r_s^2 \mathbf{H} \mathbf{H}^T + \sigma_y^2 \mathbf{I})^{-1} (\mathbf{y} - \mathbf{H} \mathbf{x}_0^*)]$$

$$\mathbf{x}_{s-1}^{\mathcal{F}} = a_s \mathbf{x}_s^{\mathcal{F}} + b_s \mathbf{F} \mathbf{x}_0^* + \sqrt{\bar{\alpha}_s} \mathbf{F} [\boldsymbol{\Sigma}_0 (\bar{\alpha}_s \boldsymbol{\Sigma}_0 + (1 - \bar{\alpha}_s) \mathbf{I})^{-1} \mathbf{H}^T (r_s^2 \mathbf{H} \mathbf{H}^T + \sigma_y^2 \mathbf{I})^{-1} (\mathbf{y} - \mathbf{H} \mathbf{x}_0^*)] \quad (72)$$

From Equation 62, we obtain

$$\mathbf{F} \mathbf{x}_0^* = c_s \mathbf{x}_s^{\mathcal{F}} + d_s \boldsymbol{\mu}_0^{\mathcal{F}} \quad (73)$$

Where:

$$c_s = \sqrt{\bar{\alpha}_s} \boldsymbol{\Lambda}_0 [\bar{\alpha}_s \boldsymbol{\Lambda}_0 + (1 - \bar{\alpha}_s) \mathbf{I}]^{-1}$$

$$d_s = (1 - \bar{\alpha}_s) [\bar{\alpha}_s \boldsymbol{\Lambda}_0 + (1 - \bar{\alpha}_s) \mathbf{I}]^{-1}$$

$$\begin{aligned}
 &= \sqrt{\bar{\alpha}_s} \mathbf{F} [\Sigma_0 (\bar{\alpha}_s \Sigma_0 + (1 - \bar{\alpha}_s) \mathbf{I})^{-1} \mathbf{H}^T (r_s^2 \mathbf{H} \mathbf{H}^T + \sigma_y^2 \mathbf{I})^{-1} (\mathbf{y} - \mathbf{H} \mathbf{x}_0^*)] \\
 &= \sqrt{\bar{\alpha}_s} [\mathbf{F} \Sigma_0 \mathbf{F}^T \mathbf{F} (\bar{\alpha}_s \Sigma_0 + (1 - \bar{\alpha}_s) \mathbf{I})^{-1} \mathbf{F}^T \mathbf{F} \mathbf{H}^T \mathbf{F}^T \mathbf{F} (r_s^2 \mathbf{H} \mathbf{H}^T + \sigma_y^2 \mathbf{I})^{-1} \mathbf{F}^T \mathbf{F} (\mathbf{y} - \mathbf{H} \mathbf{x}_0^*)] \\
 &= \sqrt{\bar{\alpha}_s} [\Lambda_0 [\bar{\alpha}_t \Lambda_0 + (1 - \bar{\alpha}_s) \mathbf{I}]^{-1} \Lambda_{h^*} \mathbf{F} (r_s^2 \mathbf{H} \mathbf{H}^T + \sigma_y^2 \mathbf{I})^{-1} \mathbf{F}^T (\mathbf{F} \mathbf{y} - \mathbf{F} \mathbf{H} \mathbf{F}^T \mathbf{F} \mathbf{x}_0^*)]
 \end{aligned} \tag{74}$$

Since:

$$\mathbf{F} (r_s^2 \mathbf{H} \mathbf{H}^T + \sigma_y^2 \mathbf{I})^{-1} \mathbf{F}^T = (r_s^2 \Lambda_{h^T} + \sigma_y^2 \mathbf{I})^{-1}$$

and denoting:

$$e_s = (r_s^2 \Lambda_{h^T} + \sigma_y^2 \mathbf{I})^{-1}$$

$$\sqrt{\bar{\alpha}_s} \mathbf{F} [\Sigma_0 (\bar{\alpha}_s \Sigma_0 + (1 - \bar{\alpha}_s) \mathbf{I})^{-1} \mathbf{H}^T (r_s^2 \mathbf{H} \mathbf{H}^T + \sigma_y^2 \mathbf{I})^{-1} (\mathbf{y} - \mathbf{H} \mathbf{x}_0^*)] = c_s \Lambda_{h^*} e_s (\mathbf{y}^{\mathcal{F}} - \Lambda_h \mathbf{F} \mathbf{x}_0^*) \tag{75}$$

Substituting Equations 75 and 73 in 72 yields:

$$\mathbf{x}_{s-1}^{\mathcal{F}} = a_s \mathbf{x}_s^{\mathcal{F}} + b_s (c_s \mathbf{x}_s^{\mathcal{F}} + d_s \boldsymbol{\mu}_0^{\mathcal{F}}) + c_s \Lambda_{h^*} e_s (\mathbf{y}^{\mathcal{F}} - \Lambda_h (c_s \mathbf{x}_s^{\mathcal{F}} + d_s \boldsymbol{\mu}_0^{\mathcal{F}}))$$

$$\mathbf{x}_{s-1}^{\mathcal{F}} = [a_s + b_s c_s - c_s \Lambda_{h^*} e_s \Lambda_h c_s] \mathbf{x}_s^{\mathcal{F}} + [b_s d_s - c_s \Lambda_{h^*} e_s \Lambda_h d_s] \boldsymbol{\mu}_0^{\mathcal{F}} + [c_s \Lambda_{h^*} e_s] \mathbf{y}^{\mathcal{F}}$$

Denoting:

$$\mathbf{G}_{\text{PIGDM}}(s) = [a_s + b_s c_s - c_s \Lambda_{h^*} e_s \Lambda_h c_s]$$

$$\mathbf{Q}_{\text{PIGDM}}(s) = [c_s \Lambda_{h^*} e_s]$$

$$\mathbf{M}_{\text{PIGDM}}(s) = [b_s d_s - c_s \Lambda_{h^*} e_s \Lambda_h d_s]$$

and get:

$$\mathbf{x}_{s-1}^{\mathcal{F}} = \mathbf{G}_{\text{PIGDM}}(s) \mathbf{x}_s^{\mathcal{F}} + \mathbf{Q}_{\text{PIGDM}}(s) \mathbf{y}^{\mathcal{F}} + \mathbf{M}_{\text{PIGDM}}(s) \boldsymbol{\mu}_0^{\mathcal{F}} \tag{76}$$

By recursively applying Equation (76) and following the same derivation steps and notation as in Appendix F, we arrive at the following closed-form distribution for  $\mathbf{x}_{0,\text{PIGDM}}^{\mathcal{F}}$ .

$$\mathbf{x}_{0,\text{PIGDM}}^{\mathcal{F}} \sim \mathcal{N}(\mathbf{D}_2 \mathbf{y}^{\mathcal{F}} + \mathbf{D}_3 \boldsymbol{\mu}_0^{\mathcal{F}}, \mathbf{D}_1^2) \tag{77}$$

## H. Additional Results: Synthetic Gaussian Distribution

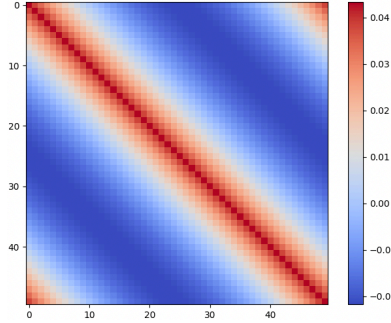


Figure 5. Covariance matrix obtained for  $d = 50$  and  $l = 0.05$ .

### H.1. IIIGDM algorithm

Here, we derive spectral recommendations for the IIIGDM algorithm under the setup introduced in Section 6.1. In the original formulation of IIIGDM, the heuristic parameter  $r_s$  plays a dual role: it both controls the uncertainty at diffusion step  $s$  and serves as a weighting term for the likelihood component in the inference equation (see Eq. 8). In that formulation, this two roles are handled through a single heuristic definition based on the diffusion noise schedule,

$$r_s = \sqrt{1 - \bar{\alpha}_s}$$

In our approach, we consider these roles separately, allowing for greater flexibility in balancing their respective influences. Specifically, we introduce a separate guidance parameter  $g_s$  while retaining  $r_s^2$  as the uncertainty-related term. The resulting inference update is given by:

$$\begin{aligned} \mathbf{x}_{s-1} = & \sqrt{\bar{\alpha}_{s-1}} \hat{\mathbf{x}}_0 + \sqrt{1 - \bar{\alpha}_{s-1}} \boldsymbol{\epsilon}_\theta(\mathbf{x}_s, s) \\ & + g_s \nabla_{\mathbf{x}_s}(\hat{\mathbf{x}}_0)^T \mathbf{H}^T ((r_s^2 \mathbf{H} \mathbf{H}^T + \sigma_y^2 \mathbf{I})^{-1})^T (\mathbf{y} - \mathbf{H} \hat{\mathbf{x}}_0) \end{aligned} \quad (78)$$

Figure 6 presents the resulting spectral recommendations for the weighting coefficients  $r_s s = 1^d$  and  $g_s s = 1^d$ , together with their mean and standard deviation computed over  $N = 5$  realizations  $\{y_i\}_{i=1}^N$ , for different numbers of diffusion steps, as described in Section 6.1. For comparison, we also include the heuristic parameter values used in the original IIIGDM algorithm.

Notably, our recommendations take into account prior information, the observed measurements, and the diffusion dynamics, while the original IIIGDM heuristics define the weighting coefficients solely based on the diffusion noise schedule.

Figure 7 compares the *Wasserstein-2* distance between the reconstructed posterior distributions and the true posterior, for both the heuristic parameter choices in IIIGDM and the proposed spectral recommendations, evaluated across multiple diffusion steps and measurement realizations  $y_i$ . We also report the distance obtained from the reconstructed posterior produced by the optimal posterior denoiser derived in (18). The spectral recommendations yield consistently lower Wasserstein distances across diffusion steps and show reduced variability across realizations compared to the IIIGDM heuristics. As expected, the exact solution achieves the lowest Wasserstein distance overall.

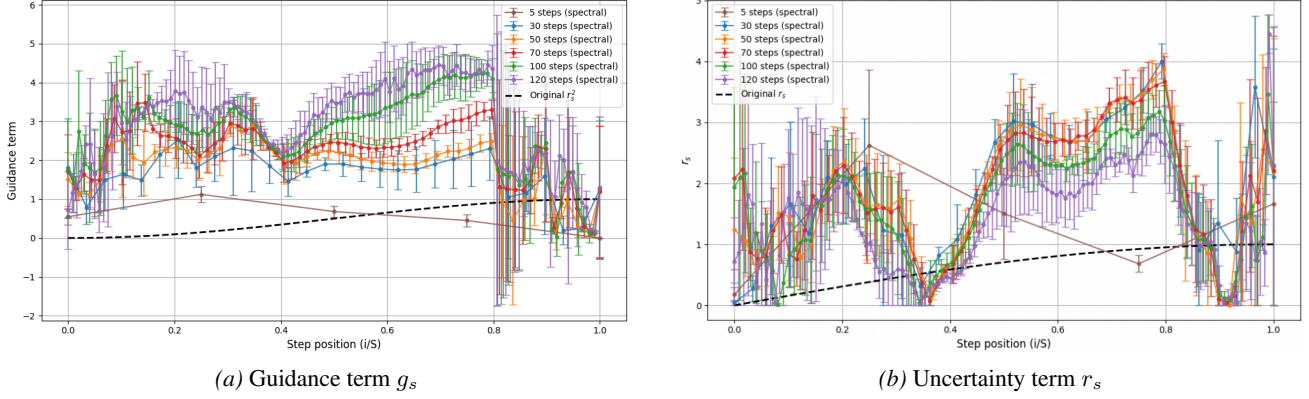


Figure 6. Figures 6a and 6b show the spectral recommendations for the IIIGDM weighting coefficients  $g_s$  and  $r_s$ , respectively. Results are shown for different diffusion step counts, with the standard deviation across realizations. The original IIIGDM heuristics indicated in black curves

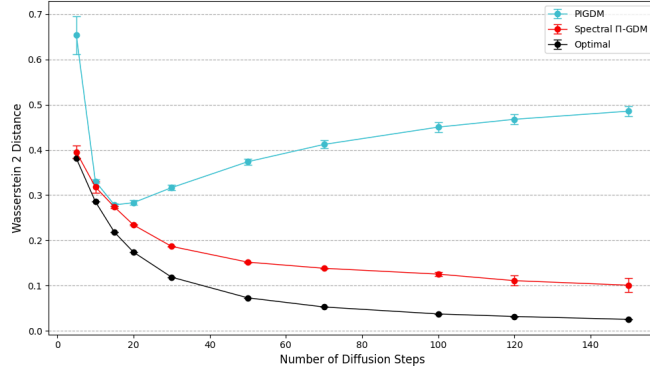


Figure 7. Comparison of the Wasserstein-2 distance for IIIGDM heuristic values, the spectral recommendations applied to IIIGDM (red), and the analytically derived ideal posterior sampler (black), across different number of diffusion steps  $S \in \{5, 10, 15, 20, 30, 50, 70, 100, 120, 150\}$ .

## I. Prior Sampling Results

### I.1. ImageNet spectral recommendation

Figure 8 shows the spectral recommendations obtained for ImageNet 256. The overall behavior is similar to that observed for FFHQ, with guidance values increasing as the diffusion process progresses; however, the absolute magnitudes differ between the two datasets. In contrast, the DPS heuristic weights remain relatively smaller and exhibit a similar trend across both datasets.

Table 3 presents a comprehensive comparison between our spectral recommendations and the original DPS heuristics. The comparison includes results on both FFHQ-256 and ImageNet-256 and considers several linear degradation settings with parameter pairs  $(\mathcal{V}, \sigma_y) \in \{(0.01, 0.1), (0.1, 0.1), (0.3, 0.1), (0.1, 0.2)\}$ . For each degradation setting, we evaluate a range of diffusion step counts  $S \in \{50, 100, 200, 300, 400\}$  thereby evaluating posterior sampling performance in regimes that also permit relatively efficient synthesis.

In this setting, selecting the DPS heuristic parameter  $\zeta'$  for the FFHQ and ImageNet datasets is non-trivial. (Chung et al., 2022a) reports recommended values that are associated with specific high numbers of diffusion steps and particular degradation settings. Guided by the methodology described in (Chung et al., 2022a), we therefore evaluated several candidate values across different step counts and selected  $\zeta' = 0.3$  for FFHQ and  $\zeta' = 0.2$  for ImageNet, falling within the range of values considered in (Chung et al., 2022a). While smaller values resulted in insufficient measurement fidelity, larger values led to unstable behavior in the final reconstructions. This sensitivity underscores the advantage of the proposed spectral recommendations, which eliminate the need for repeated heuristic tuning.

All experiments were conducted using the implementation and pretrained models from (Chung et al., 2022a). While some reported values differ from those in (Chung et al., 2022a), this discrepancy is attributable to the use of fewer diffusion steps

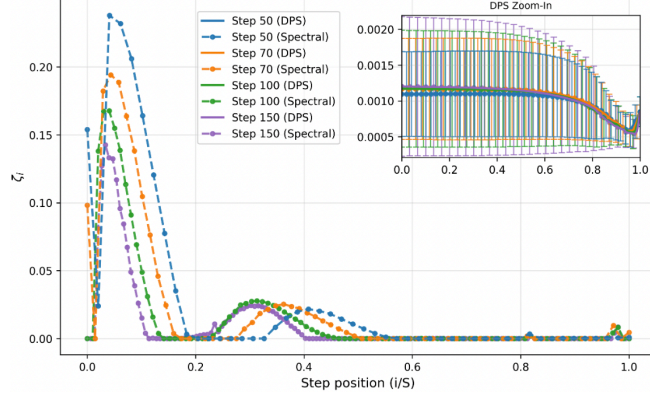


Figure 8. Comparison of spectral recommendations on the ImageNet 256 dataset, with a zoomed-in view of the DPS heuristics for selected diffusion steps  $S \in \{50, 70, 100, 150\}$ .

and different degradation settings.

Table 3 reports results across four evaluation metrics, SSIM, PSNR, LPIPS, and FID, reflecting measurement fidelity and perceptual quality. Overall, the spectral recommendations tend to achieve a more balanced tradeoff between these two aspects compared to the original DPS heuristics.

In some settings with a small number of diffusion steps, the DPS heuristic attains lower FID values; however, this is typically accompanied by reduced performance on measurement fidelity metrics. This behavior may be related to the small guidance step sizes commonly used by DPS, which can yield visually plausible samples that are less strongly constrained by the noisy measurements when using fewer diffusion steps. Representative examples are shown in Figure 9.

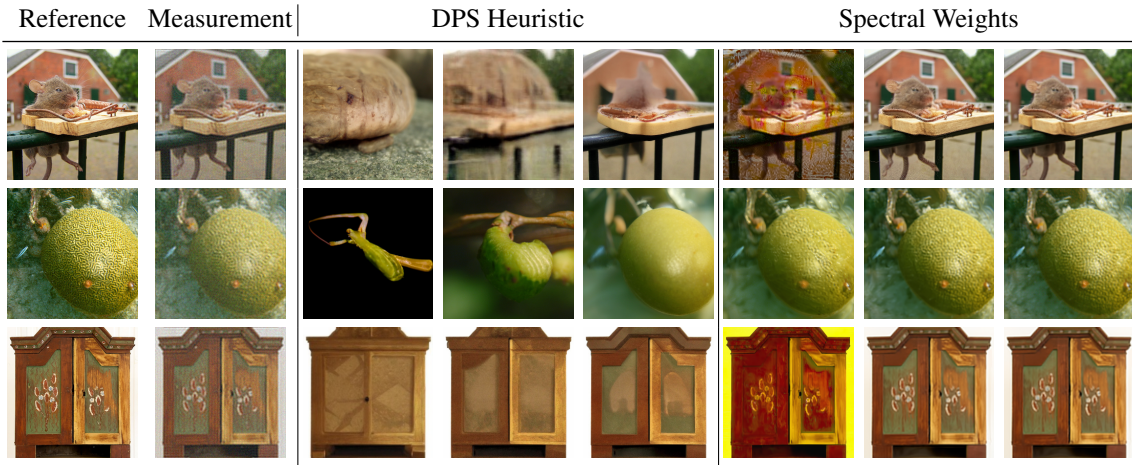


Figure 9. Qualitative comparison of visual results on ImageNet. Each row shows the reference image, the degraded measurement, samples obtained using the DPS heuristic at 100, 200, and 400 diffusion steps (from left to right), and samples obtained using the proposed spectral recommendations at the same step counts.

Figure 9 compares visual results obtained using the DPS heuristic and the proposed spectral recommendations under a degradation with  $\mathcal{V} = 0.1$  and  $\sigma_y = 0.1$ , across different numbers of diffusion steps  $S \in \{100, 200, 400\}$ .

For a small number of diffusion steps, the DPS heuristic produces visually plausible images; however, these reconstructions often deviate from the reference images in terms of both global structure and fine details. In contrast, the spectral recommendations yield visual results that more closely align with the reference images and the measurements, although they may exhibit minor effects such as localized color variations. This behavior helps explain why the DPS heuristic can attain favorable FID values at low step counts while showing reduced measurements fidelity.

As the number of diffusion steps increases, the DPS heuristic increasingly incorporates information from the measurements, leading to visual results that more closely resemble the reference images, although deviations remain due to the limited

heuristic step size. At the same time, the spectral recommendations produce visually natural outputs that remain consistent with the measurements. This convergence in behavior aligns with the quantitative trends reported in Table 9, where the spectral recommendations exhibit a balanced tradeoff between perceptual quality and measurement fidelity.

Figure 10 shows additional visual results on the ImageNet dataset, evaluated at 500 diffusion steps. While the DPS heuristic produces visually natural patterns, some differences with respect to the measurements remain. By comparison, the spectral recommendations yield visually natural samples that are more consistently aligned with the measurements, including at finer levels of detail.

Table 3. Quantitative comparison between the proposed spectral recommendations and the DPS heuristic. Results are reported on FFHQ-256 and ImageNet-256 across multiple degradation settings  $(\mathcal{V}, \sigma_y)$  and diffusion step counts, using PSNR, SSIM, LPIPS, and FID.

$\mathcal{V}$	$\sigma_y$	METHOD	STEPS	FFHQ 256				IMAGENET 256			
				PSNR↑	SSIM↑	LPIPS↓	FID↓	PSNR↑	SSIM↑	LPIPS↓	FID↓
1%	0.1	SPECTRAL	50	<b>11.32</b>	<b>0.26</b>	0.71	197.83	8.10	0.12	0.73	283.29
			100	<b>13.24</b>	<b>0.29</b>	<b>0.67</b>	171.32	11.85	<u>0.24</u>	0.68	184.89
			200	<b>16.27</b>	<b>0.34</b>	<b>0.60</b>	<b>133.89</b>	<b>16.04</b>	<b>0.30</b>	<b>0.60</b>	174.88
			300	<b>17.18</b>	<b>0.37</b>	<b>0.59</b>	<b>132.80</b>	<b>14.01</b>	<b>0.28</b>	<b>0.64</b>	<b>137.44</b>
			400	<b>18.27</b>	<b>0.39</b>	<b>0.57</b>	<b>121.08</b>	<b>15.09</b>	<b>0.29</b>	<b>0.62</b>	<b>144.01</b>
	0.1	DPS	50	4.59	0.24	<b>0.52</b>	<b>169.29</b>	<b>12.55</b>	<b>0.24</b>	<b>0.68</b>	<b>132.02</b>
			100	12.47	0.28	0.68	<b>155.47</b>	<b>12.01</b>	<u>0.24</u>	<b>0.67</b>	<b>142.94</b>
			200	13.53	0.30	0.66	142.03	11.83	<u>0.24</u>	0.66	<b>147.25</b>
			300	14.56	0.33	0.64	137.69	11.94	0.24	0.66	144.88
			400	14.68	0.33	0.63	137.13	11.94	0.25	0.66	144.08
10%	0.1	SPECTRAL	50	<b>16.10</b>	<b>0.46</b>	<b>0.61</b>	<b>140.88</b>	<b>15.99</b>	<b>0.41</b>	<b>0.59</b>	262.73
			100	<b>16.87</b>	<b>0.49</b>	<b>0.58</b>	130.05	10.22	<b>0.40</b>	<b>0.58</b>	231.42
			200	<b>17.89</b>	<b>0.51</b>	<b>0.53</b>	107.91	<b>15.67</b>	<b>0.41</b>	<b>0.55</b>	<b>120.55</b>
			300	<b>21.37</b>	<b>0.59</b>	<b>0.45</b>	<b>79.2</b>	<b>14.56</b>	<b>0.37</b>	<b>0.58</b>	<b>139.86</b>
			400	<b>22.35</b>	<b>0.61</b>	<b>0.42</b>	<b>68.3</b>	<b>13.92</b>	<b>0.35</b>	<b>0.60</b>	<b>54.22</b>
	0.1	DPS	50	11.99	0.28	0.70	145.99	12.73	0.26	0.68	<b>130.60</b>
			100	14.06	0.35	0.63	<b>120.52</b>	<b>12.41</b>	0.27	0.67	<b>142.66</b>
			200	16.65	0.43	0.55	<b>97.04</b>	12.55	0.28	0.66	143.66
			300	18.11	0.47	0.51	87.79	12.92	0.29	0.64	141.28
			400	19.18	0.5	0.49	82.26	13.29	0.31	0.63	131.13
30%	0.1	SPECTRAL	50	<b>15.65</b>	<b>0.42</b>	<b>0.57</b>	127.92	<b>13.00</b>	<b>0.38</b>	<b>0.67</b>	159.37
			100	<b>17.28</b>	<b>0.49</b>	<b>0.53</b>	111.52	9.33	0.23	0.69	233.26
			200	<b>20.42</b>	<b>0.58</b>	<b>0.45</b>	87.91	10.06	0.23	0.67	288.89
			300	<b>26.11</b>	<b>0.72</b>	<b>0.32</b>	<b>48.52</b>	<b>13.56</b>	<b>0.39</b>	<b>0.57</b>	<b>127.28</b>
			400	<b>22.13</b>	<b>0.63</b>	<b>0.41</b>	<b>70.67</b>	<b>15.74</b>	<b>0.44</b>	<b>0.58</b>	<b>120.33</b>
	0.1	DPS	50	12.60	0.33	0.65	<b>121.45</b>	12.76	0.26	0.68	<b>129.48</b>
			100	14.93	0.42	0.56	<b>98.23</b>	<b>12.25</b>	<b>0.27</b>	<b>0.67</b>	<b>143.77</b>
			200	<b>18.29</b>	<b>0.53</b>	<b>0.47</b>	<b>78.64</b>	<b>12.88</b>	<b>0.30</b>	<b>0.65</b>	<b>144.45</b>
			300	19.45	0.57	0.44	75.50	12.96	0.31	0.64	133.54
			400	20.34	0.59	0.42	71.49	13.72	0.33	0.62	132.72
10%	0.2	SPECTRAL	50	<b>14.56</b>	<b>0.42</b>	<b>0.65</b>	<b>144.32</b>	<b>14.73</b>	<b>0.37</b>	<b>0.64</b>	152.59
			100	<b>15.73</b>	<b>0.45</b>	<b>0.59</b>	<b>120.04</b>	<b>14.81</b>	<b>0.37</b>	<b>0.63</b>	152.18
			200	<b>18.72</b>	<b>0.50</b>	<b>0.50</b>	<b>85.81</b>	<b>14.83</b>	<b>0.38</b>	<b>0.62</b>	145.89
			300	<b>23.35</b>	<b>0.58</b>	<b>0.41</b>	<b>57.94</b>	<b>14.52</b>	<b>0.37</b>	<b>0.64</b>	<b>137.42</b>
			400	<b>22.69</b>	<b>0.55</b>	<b>0.44</b>	<b>61.74</b>	<b>16.42</b>	<b>0.42</b>	<b>0.57</b>	<b>120.90</b>
	0.2	DPS	50	11.95	0.28	0.69	144.70	12.96	0.26	0.68	<b>125.55</b>
			100	13.85	0.34	0.63	120.49	12.58	0.27	0.67	<b>139.52</b>
			200	17.08	0.43	0.54	91.55	12.44	0.28	0.66	<b>141.26</b>
			300	17.63	0.45	0.53	88.43	12.90	0.29	0.65	137.63
			400	18.64	0.49	0.50	82.39	13.12	0.30	0.64	136.29

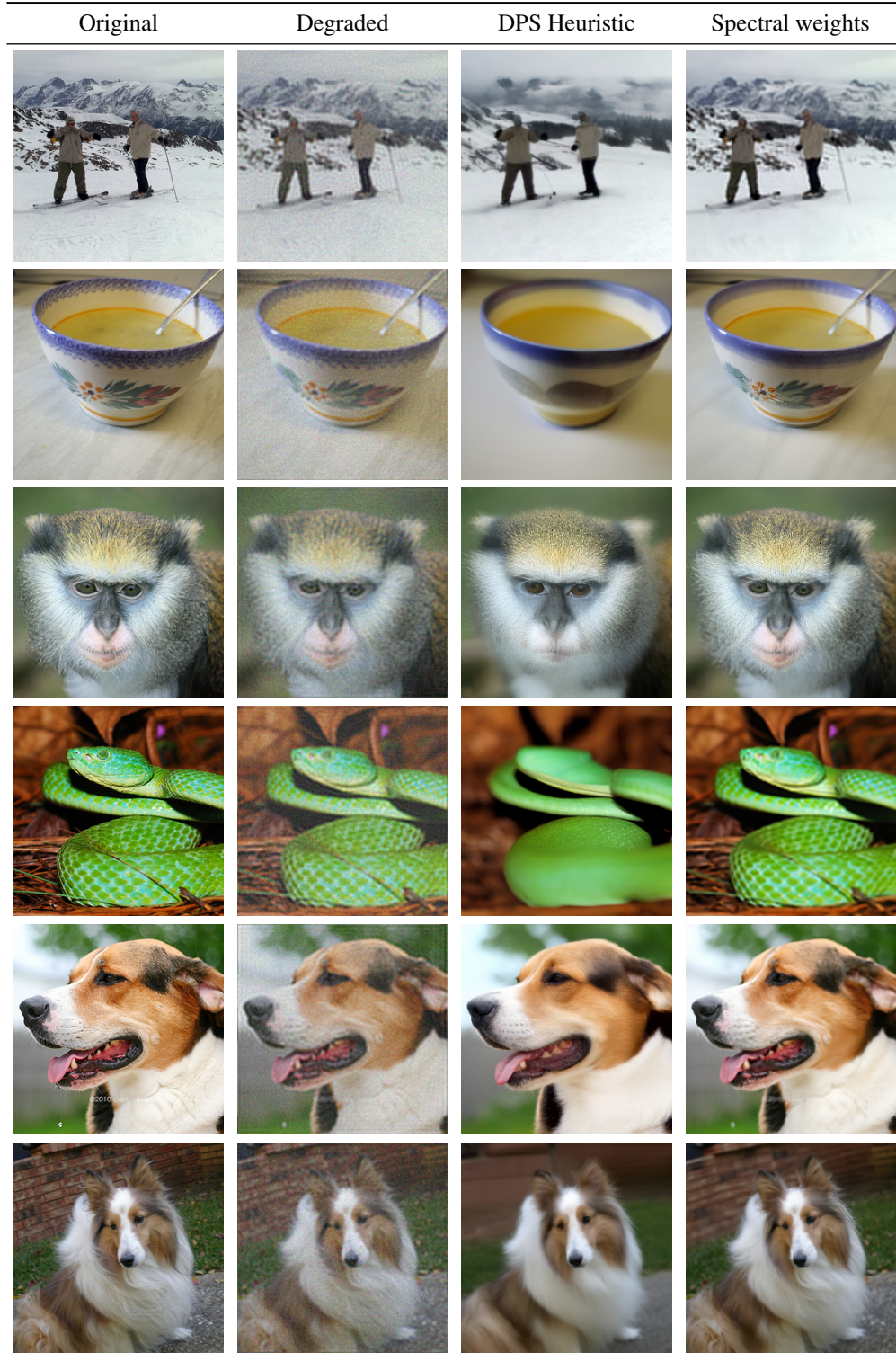


Figure 10. Qualitative comparison of visual results on the ImageNet dataset. Each row shows the reference image, the degraded observation with  $\mathcal{V} = 0.1$  and  $\sigma_y = 0.1$ , and samples obtained using the DPS heuristic and the proposed spectral weighting, both evaluated at 500 diffusion steps.

## J. Posterior Sampling Results

This section includes further analysis of posterior behavior under fixed observations. As described in Section 6.2, for three realizations  $\mathbf{x}_i$  we generate corresponding degraded observations  $\mathbf{y}_i$  and produce 1,000 reconstructions for each case. Evaluation metrics are computed separately for each realization and then averaged.

Table 4 reports the resulting metrics. Here, *Spectral* denotes results obtained using spectral recommendations derived by solving the optimization problem 17, which captures expected posterior behavior across degraded measurements and is solved once for a fixed degradation operator. In contrast, *Spectral K=1* corresponds to solving the optimization problem independently for each realization. Overall, both spectral strategies tend to achieve more favorable performance in terms of measurement fidelity and perceptual similarity compared to the DPS heuristic. In addition, solving the optimization problem separately for each realization yields slightly improved results, reflecting the benefit of adapting the weighting to the specific observation.

Table 4. Quantitative results for posterior sampling under fixed observations.

Method	Steps	PSNR $\uparrow$	SSIM $\uparrow$	LPIPS $\downarrow$
DPS	50	12.52	0.27	0.69
	100	14.99	0.35	0.61
	200	18.15	0.44	0.52
	300	19.88	0.49	0.48
	400	21.04	0.53	0.45
	500	21.89	0.55	<b>0.43</b>
Spectral	50	<b>16.63</b>	<b>0.48</b>	<b>0.60</b>
	100	<u>17.55</u>	<u>0.51</u>	<u>0.56</u>
	200	<u>19.01</u>	<u>0.53</u>	<u>0.52</u>
	300	<u>23.05</u>	<u>0.62</u>	<b>0.43</b>
	400	<u>23.47</u>	<u>0.61</u>	<u>0.42</u>
	500	<u>22.07</u>	<u>0.61</u>	<u>0.45</u>
Spectral K=1	50	12.95	0.38	0.66
	100	<b>18.48</b>	<b>0.53</b>	<u>0.53</u>
	200	<b>22.24</b>	<b>0.59</b>	<u>0.44</u>
	300	<b>23.08</b>	<u>0.62</u>	<b>0.41</b>
	400	<b>24.76</b>	<b>0.63</b>	<b>0.39</b>
	500	<b>22.72</b>	<u>0.61</u>	0.44

Figures 11 and 12 present qualitative comparisons for two different images. In each figure, the top row shows the reference image on the left and the corresponding degraded observation on the right. Each subsequent row corresponds to a different weighting scheme: DPS (top), the proposed spectral recommendations (middle), and the realization-specific spectral variant with  $k=1$  (bottom). Within each row, posterior samples obtained with 100, 200, and 400 diffusion steps are shown from left to right. For visualization purposes, each example was selected from the 1,000 generated samples by choosing the instance that best preserves visual naturalness while remaining consistent with the reference image.

As illustrated in Figures 11 and 12, For a small number of diffusion steps, the DPS heuristic produces samples that reflect the global structure of the reference image, while remaining less constrained by the measurements. In contrast, the spectral recommendations yield samples that adhere more closely to the observed data. We also observe variability across samples produced by all weighting schemes, indicating that the methods do not converge to a single estimate such as the posterior mean.

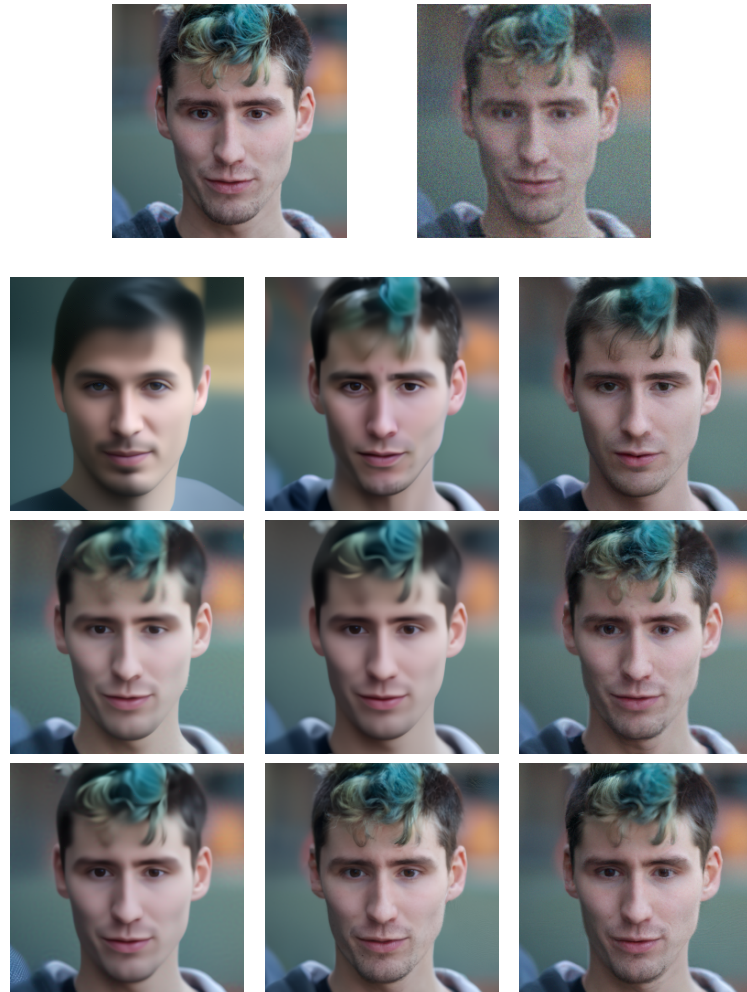


Figure 11. Qualitative comparison of posterior samples under a fixed observation. The top row shows the reference image (left) and the corresponding degraded observation (right). Subsequent rows present reconstructions using different guidance schemes: the DPS heuristic (top), spectral recommendations (middle), and the realization-specific spectral variant with  $k = 1$  (bottom). Samples corresponding to 100, 200, and 400 diffusion steps are shown from left to right.

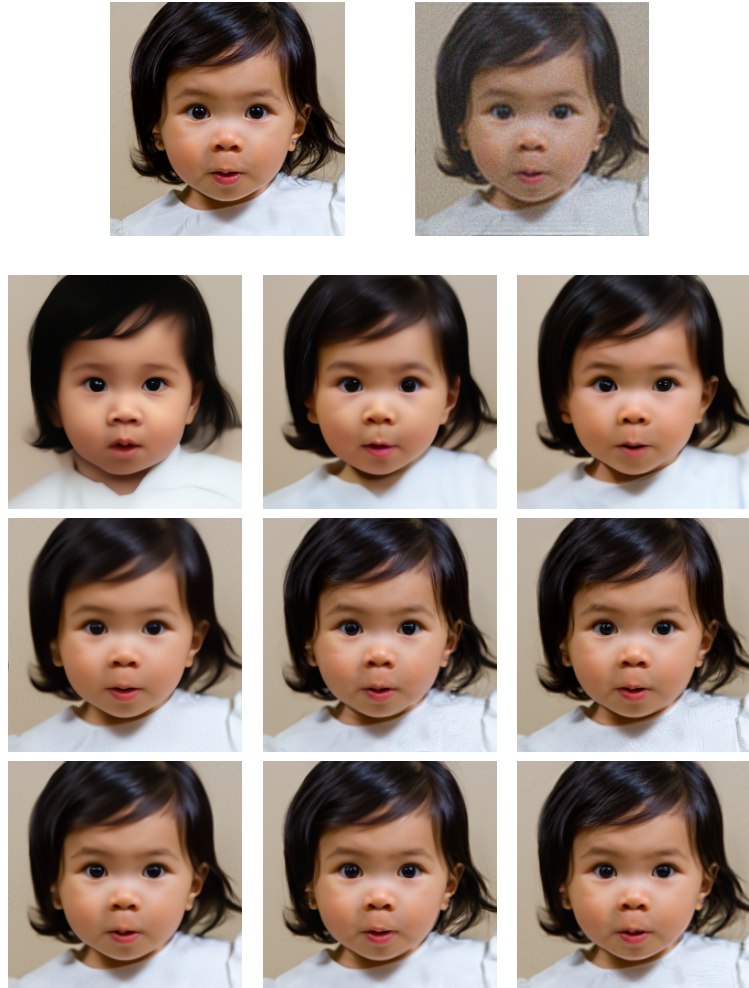


Figure 12. Qualitative comparison of posterior samples under a fixed observation. The top row shows the reference image (left) and the corresponding degraded observation (right). Subsequent rows present reconstructions using different guidance schemes: the DPS heuristic (top), spectral recommendations (middle), and the realization-specific spectral variant with  $k = 1$  (bottom). Samples corresponding to 100, 200, and 400 diffusion steps are shown from left to right.

## K. Covariance matrix Estimation

Under stationarity, the covariance matrix of a color image  $\mathbf{x}_0 \in \mathbb{R}^{3N}$  has block-circulant with circulant blocks (BCCB) structure:

$$\Sigma_0 = \begin{pmatrix} \Sigma_{RR} & \Sigma_{RG} & \Sigma_{RB} \\ \Sigma_{GR} & \Sigma_{GG} & \Sigma_{GB} \\ \Sigma_{BR} & \Sigma_{BG} & \Sigma_{BB} \end{pmatrix}.$$

Consequently, each block is diagonalized by the 2D discrete Fourier transform. Let  $\mathbf{F}_N$  denote the unitary 2D DFT matrix; then

$$\Sigma_{ij} = \mathbf{F}_N^* \Lambda_{ij} \mathbf{F}_N,$$

where  $\Lambda_{ij}$  are diagonal matrices containing the auto- and cross-channel power spectra.

This yields the Fourier-domain representation of the full covariance

$$\Sigma_0 = (\mathbf{I}_3 \otimes \mathbf{F}_N^*) \Lambda_0 (\mathbf{I}_3 \otimes \mathbf{F}_N),$$

where  $\Lambda$  is block-diagonal across spatial frequencies.

This spectral representation allows the optimization problem from Section 3 to be applied, and solved using the acceleration approaches described in Appendix L.

## L. Optimization Time Analysis

The computational cost of solving the proposed optimization problem is influenced by several factors, including the signal resolution and the number of diffusion steps. An additional consideration is whether the optimization is performed separately for each measurement realization  $\mathbf{y}_i$  (Equation (16)), yielding realization-specific improvements across metrics, or whether a single optimization is solved once for a given degraded system (Equation (16)), and then reused across realizations.

To accelerate the optimization procedure, we adopt two principles introduced in (Benita et al., 2025). The first is *iterative optimization*, in which the problem is solved progressively: the process starts with a small number of diffusion steps, allowing fast convergence with relatively low computational requirements. The resulting solution is then interpolated to the appropriate length and used to initialize the optimization with a larger number of steps.

The second principle is *dimensionality reduction*. For high-resolution signals, computational requirements increase significantly; therefore, a low-rank covariance approximation is assumed. Specifically, only the  $d$  most significant eigen-directions are retained using principal component analysis (PCA), while components associated with near-zero eigenvalues are discarded. Together, these methods substantially reduce optimization time without compromising performance.

Table 5 reports the solution times of the optimization problem on the FFHQ dataset at a resolution of  $256 \times 256 \times 3$ , using iterative initialization and dimensionality reduction. All experiments are conducted on a standard CPU using the L-BFGS-B via SciPy, with the maximum number of optimization iterations set to 2500 and a function tolerance of  $10^{-6}$ .

Table 5. Optimization time as a function of the number of diffusion steps for the FFHQ dataset ( $256 \times 256 \times 3$ ). Results are obtained using iterative initialization and dimensionality reduction

Number of diffusion steps	Optimization time (seconds)
10	1.77
50	13.73
100	32.40
200	393.30
300	189.71
400	333.50
600	997.22
800	1406.56
1000	1902.48

Table 5 shows that the time required to solve the optimization problem increases with the number of diffusion steps. However, when the optimization is performed once per degradation setting, the resulting computation time remains within a practical range, as the same spectral recommendations can be reused across multiple inference runs for that setting.